An Integrated Lumped Parameter-CFD approach for off-design ejector performance evaluation

Giorgio Besagni *, Riccardo Mereu, Paolo Chiesa, Fabio Inzoli

Politecnico di Milano, Department of Energy, Via Lambruschini 4, 20156 Milan, Italy

Received 9 May 2015
Accepted 10 August 2015

1. Introduction

Ejector is a simple component: a primary flow enters in a primary nozzle, entrains the secondary flow from a suction chamber, they mix and a diffuser compresses the stream (Fig. 1, Table 1). The ejector thus provides entrainment, mixing and compression, making it suitable for fuel cell recirculation, refrigeration cycles and energy conversion systems. The efficiency of these systems is highly dependent on the ejector efficiency and accurate models are needed for both on-design and off-design ejector performance prediction [1,2]: a small deviation from the optimum operating conditions of the ejector might drastically lower the performances of the whole system. In the literature, Lumped Parameter Models (LPMs) and Computational Fluid-Dynamics (CFD) models have been proposed, developed and applied [3].

The lumped parameter models found in the literature have been mainly developed for supersonic ejectors in refrigeration cycles. Only a few studies concerning subsonic ejectors are present, despite of interest for energy applications (i.e., exhaust gas in industrial plants [4] and fuel cells [5–8]). Most of the models in the literature use extensions of the approach of Keenan et al. [9] considering local flow behavior by using assumption on the local flow structures [5,10–13] and introducing ejector component effi-ciencies [3,14]. The values of these efficiencies highly influence the accuracy of ejector lumped parameter models [15–17] and are gen-erally taken as constant, even if their value depends on the geom-etry, the working fluid, and the operating conditions [18,19]. In order to improve the performance of lumped parameter models (especially when considering the off-design operating conditions), these values should take into account the local flow phenomena

* Corresponding author.
E-mail addresses: giorgio.besagni@polimi.it (G. Besagni), riccardo.mereu@polimi.it (R. Mereu), paolo.chiesa@polimi.it (P. Chiesa), fabio.inzoli@polimi.it (F. Inzoli).

Nomenclature

Symbols

A	area, m^2
c	sonic velocity, m/s
h	specific enthalpy, kJ/kg
I	turbulence intensity, %
ρ	density, kg/m^3
m	mass flow rate, kg/s
$m_{s,as}$	parameter used and define din Table 8; $m_{s,ad} = \frac{\dot{m}_s (R*T_s)^{0.5}}{p_s A_{s,out}}$, –
M	mach number, –
MM	molar mass, kg/kmol
p	pressure, Pa
R	gas constant, kJ/kmol K
R^*	specific gas constant R/MM, kJ/kg K
Re	Reynolds number, –
T	temperature, K
v	velocity, m/s
w	ejector width, m
x	axial coordinate, m
y	axial distance, m
y_{wall}	wall distance from axis, m
y^+	turbulent parameter, –
Y^*	y/y_{wall}, –
Z	*parameter used and defined in* Table 8; $Z = \omega\left(\frac{p_{mix}}{p_s}\right)^{0.02}$
Z'	*parameter used and defined in* Table 8; $Z' = \left(\frac{d_t}{d_{mix}}\right)^{0.1}(1+\omega)^{0.35}$

Subscripts

0	total conditions
d	diffuser
in	ejector inlet
is	isentropic condition
mix	mixing zone
out	ejector outlet
p	primary nozzle
s	suction chamber
t	nozzle throat section

Greek letters

β	compression ratio of the secondary flow in the suction chamber ($p_{s,in}/p_{s,t}$)
η	efficiency
ω	entrainment ratio; $\omega = \dot{m}_s/\dot{m}_p$, –
μ	molecular viscosity
μ_t	turbulent viscosity
γ	heat capacity ratio
φ_p	$p_{0p,in}/p_{out}$
φ_s	$p_{0s,in}/p_{out}$
ζ	generic variable in Navier–Stokes equations

Acronyms

CAM	Constant Area Mixing
CFD	Computational Fluid Dynamics
CFL	Courant–Friedrichs–Lewy
CPM	Constant Pressure Mixing
EWT	Enhanced wall treatment
ILPM-CFD	Integrated Lumped Parameter-CFD Model
LPM	Lumped Parameter Model
LPM-CE	Lumped Parameter Model with Constant Efficiencies
PEMFC	Proton Exchange Membrane Fuel Cell
RANS	Reynolds-Averaged Navier–Stokes
SOFC	Solid Oxide Fuel Cell
SWF	Standard Wall Function

[20]. The prediction of ejector local flow phenomena is actually matter of intensive research and is usually approached by using Computational Fluid-Dynamics (CFD) analysis.

The Computational Fluid-Dynamics models have been studied in the last decades and are mainly based on the Reynolds Averaged Navier Stokes (RANS) approach [3,21–25]. CFD models are generally validated with global data (i.e., the entrainment ratio, ω), but a validation using local data should be preferred, due to the flow phenomena inside the ejector (i.e., shock waves, under-expanded jet and flow separations [26,27]). Furthermore, the results of the CFD models highly depend upon the turbulence model used, requiring the evaluation of different models before apply the numerical modeling to a broad range of operating conditions [28,29]. A CFD approach, if properly validated, could be used for optimizing the geometry, for providing an insight view of the local flow phenomena and for improving LPMs performance. In the recent years, the use of CFD for improving the performance of lumped parameter models was matter of intensive study [1,5,6,8]. In the present paper, we contribute to the discussion proposing a method for integrating CFD and lumped parameter models.

The main goal of this paper is to improve the accuracy of lumped parameter models introducing a formulation for ejector efficiencies as a function of the local phenomena predicted by CFD modeling. The concept of variable efficiency formulations for improving lumped parameter models accuracy has been initially

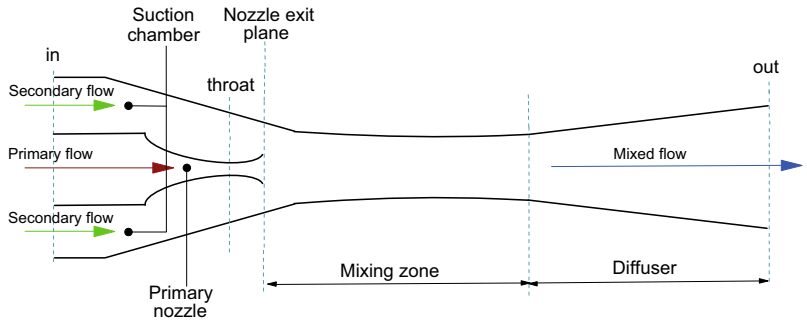

Fig. 1. Ejector layout.

Table 1
Ejector classification.

Parameter	Condition	Classification
Nozzle shape	Convergent	Subsonic ejector
	Convergent–divergent	Supersonic ejector
Nozzle exit position	Inside suction chamber	Constant Pressure Mixing ejector (CPM)
	Inside constant area zone	Constant Area Mixing ejector (CAM)
Number of fluid phases	Single phase flow inside ejector	Single phase ejector
	Two phase flow inside ejector	Two phase ejector

proposed in the review of He et al. [3], later remarked in the review of Chen et al. [30] and in the studies of Besagni et al. [16,20]. A variable formulation for the ejector efficiencies can be obtained by literature data [17], experimental investigations [18] or CFD analysis [19,20]. This paper focuses on a convergent nozzle ejector and proposes a lumped parameter model with variable efficiencies provided by a CFD analysis. The CFD approach is used for studying a broad range of operating conditions and building ejector efficiency maps relating the ejector component efficiencies to local flow quantities. Using these maps, the CFD and LPM techniques are coupled for building an Integrated LPM-CFD (ILPM-CFD) approach. The proposed approach can couple the advantages of both LPM and CFD. In the development of the integrated approach, an important point is the validation of the CFD approach and, as stated above, the evaluation of the RANS turbulence models. For this reason, in this paper, a benchmark with global and local data is selected and used for evaluating seven RANS turbulence models, before studying the ejector efficiencies.

The paper is structured as follows. In Section 2, the benchmark used is presented and the CFD approach is discussed. In Section 3, the CFD approach is validated and RANS models are compared and evaluated. In Section 4, the lumped parameter model is presented and the ejector component efficiencies are defined. In Section 5, the CFD approach is used to determine ejector component efficien-cies, to investigate the influence of the flow phenomena over ejec-tor efficiencies and to build the efficiency maps. In Section 6, the Integrated LPM-CFD (ILPM-CFD) model is built introducing the ejector efficiency maps into the lumped parameter model. The ILPM-CFD model is validated and compared with constant efficiency models, showing better performance and a wider range of applicability. Finally, conclusions are outlined and the future studies are described.

2. CFD model

The benchmark used for the CFD model validation process is the study of Gilbert and Hill [31], focused on the turbulent flow through a symmetric air–air ejector with rectangular cross-section (Fig. 2). For the detailed description of the geometry (i.e., the suction chamber profile), the reader should refer to the original reference. The flow field analyzed concerns a moderately under expanded jet. The experimental dataset consists in velocity and temperature values along the axis of the ejector for a number of operating conditions (defined as "run 6, 7, 9, 10" and presented in Table 2). All these runs have been used for the validation process.

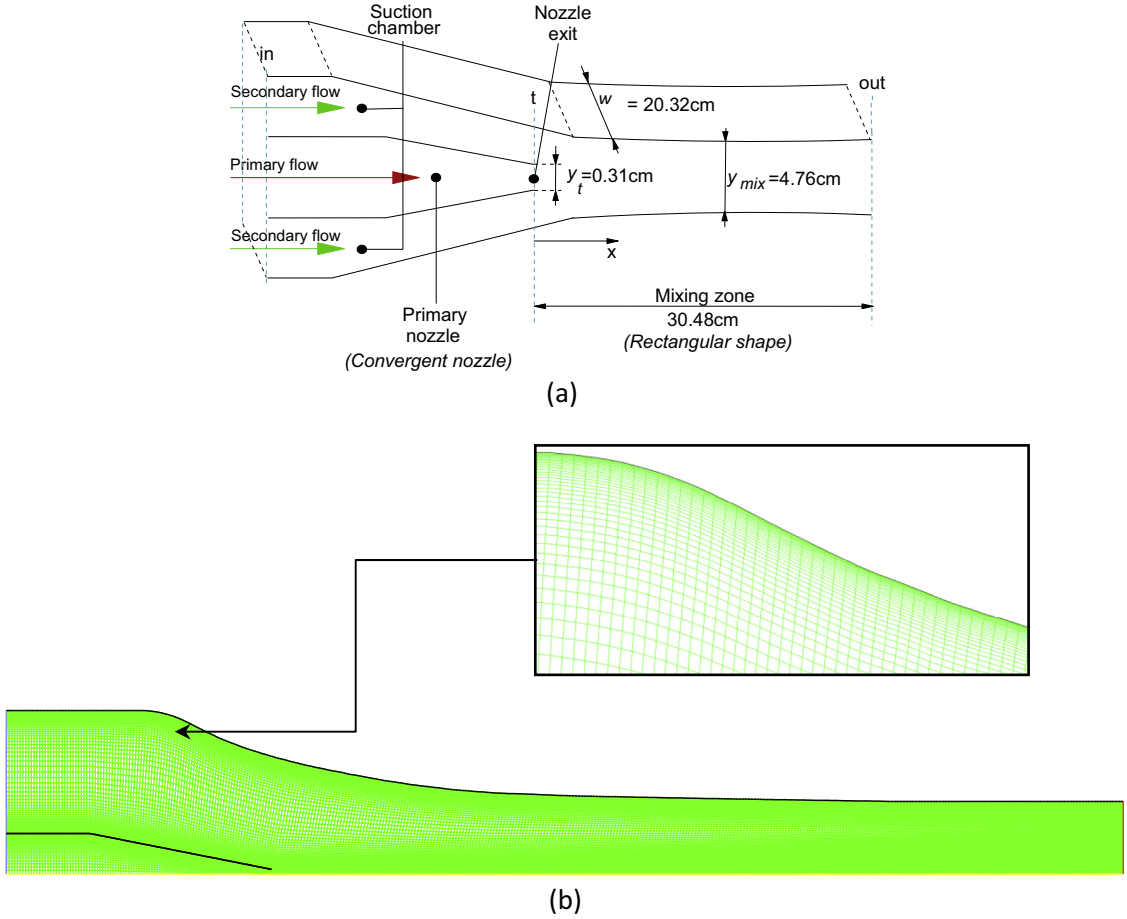

Fig. 2. Ejector studied: (a) geometrical details and (b) mesh employed.

Table 2
Cases tested: operating conditions.

Case	Entrainment ratio[a] (–)	Parameter	Primary flow	Secondary flow	Mixing outlet
Run 6	3.91	Temperature (K)	360.6	303.9	–
		Mass flow rate (kg/s)	1.58	6.17	–
		Pressure (Pa)	246,832	102,042	99,700
Run 7	4.17	Temperature (K)	359.4	301.7	–
		Mass flow rate (kg/s)	1.58	6.59	–
		Pressure (Pa)	246,832	102,042	98,100
Run 9	4.66	Temperature (K)	357.8	305.6	–
		Mass flow rate (kg/s)	1.58	7.37	–
		Pressure (Pa)	246,350	101,560	92,700
Run 10	5.01	Temperature (K)	366.7	303.9	–
		Mass flow rate (kg/s)	1.56	7.81	–
		Pressure (Pa)	246,143	101,353	92,700

[a] $\dot{m}_s/\dot{m}_p$.

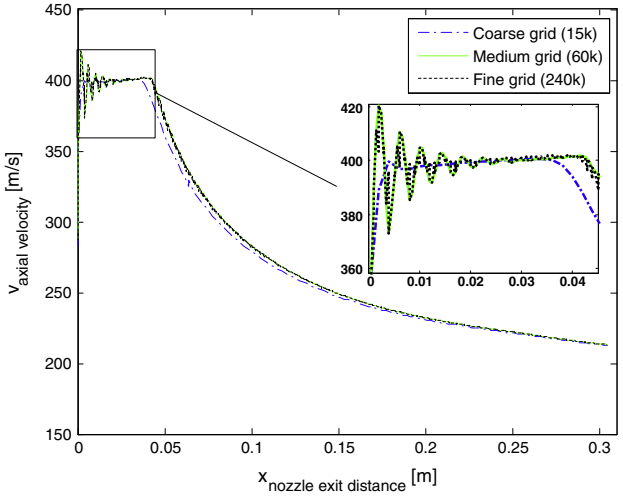

Fig. 3. Grid analysis on three different meshes using the k–ω SST model (Run 9).

2.1. Meshing approach

A 2D symmetric domain was used for modeling the ejector, based on its symmetric nature. The two-dimensional domain was possible because of the high ejector aspect ratio and the suction chamber in the experimental setup (for the secondary flow at the mixing chamber corners). Quadrilateral elements were used for minimizing the numerical diffusion. Furthermore, numerical errors may also depend on the mesh quality [32] and the criteria used in this study to limit them were: (i) maximum skewness below 0.5,(ii) orthogonally higher than 0.75 and (iii) maximum growth rate 20%. The mesh was refined on the mixing layer and near-wall regions.

The independence of the results from the grid has been analyzed obtaining a resulting grid composed by 60,000 quadrilateral elements. Three meshes were used to evaluate the grid independency of the simulation: a coarse (approx. 15,000 cells), a medium (about 60,000 cells), and a fine (approx. 240,000 cells) one. The centerline velocity values are presented in Fig. 3. The mesh was refined during the simulations on the basis of the gradient of the Mach number.

2.2. Numerical setting

The finite volume commercial code ANSYS-Fluent rel.13.0 has been adopted for solving and energy, momentum and mass conservation equations [33]. The compressible flow determines a strong coupling between the equations and a coupled solver has been adopted. In this numerical approach, even if a steady case is investigated, the time marching is assumed to proceed until a time-invariant solution is obtained. For this reason, the coupled algorithm includes the Courant–Friedrichs–Lewy (CFL) number to be set (in this case set to 1). Spatial discretization is treated by using numerical schemes of high order (the MUSCL scheme [33]) to limit the numerical diffusion, the time discretization is instead treated by using an Euler implicit scheme and second order schemes are also used for the turbulence quantities.

2.2.1. Turbulence and near-wall-treatment modeling

In this study, the most widely used RANS turbulence models have been compared and evaluated: Spalart–Allmaras, k–ε Standard, k–ε RNG, k–ε Realizable, k–ω Standard, k–ω SST and linear RSM (Reynolds-Stress-Model). All these models have been used in their original implementation without further modifications, in order to guarantee their use and application to all users and avoid reducing their generality. The chosen models have been widely used in literature for ejectors demonstrating their appropriateness for this kind of application (i.e., Bartosiewicz et al. [28,34], Besagni et al. [4], Bouhanguel et al. [35], Dvorak and Vit [36], Kolar and Dvorak [37], Gagan et al. [29]).

A preliminary study was conducted on the wall treatment and a sensitivity analysis has been performed on two different meshes: the medium mesh (described above) with initial grid point spacing ranging from $y^+ = 15$ to $45 \approx 35$, and the fine mesh ($y^+ < 1 \approx 0.25$ to 0.75), derived from the medium one refining the region near the wall boundaries. The first mesh has been used for studying different wall-function models: (i) Standard-Wall-Function (SWF), (ii) Scalable-Wall-Function, and (iii) Non-Equilibrium-Wall-Function. The second mesh has been employed for studying the influence of Enhance Wall Treatment (EWT) use. It is worth noting that the k–ω SST, k–ω, and Spalart–Allmaras models do not include a wall function because of their formulation. The k–ε Standard, k–ε RNG, k–ε Realizable, and linear RSM models require a near-wall-treatment modeling.

Table 3 presents the differences in terms of static pressure between the primary flow inlet and the ejector outlet. These results are presented for the different turbulence models, meshes and near-wall-treatment approaches tested here. The results have shown that:

- **Medium mesh.** All the wall treatments provide similar results: the differences between each result were below the 1%. It is worthy notice that was not easy to reach a converged solution with the k–ε Standard along with the Non-Equilibrium-Wall-Function. The Non-Equilibrium-Wall-Function could be

Table 3
Wall treatment: difference in static pressures $\Delta p = p_{p,in} - p_{out}$ (Pa) (Run 9).

Mesh	Wall treatment	k–ε Standard	k–ε Realizable	k–ε RNG	k–ω Standard	k–ω SST	RSM	Spalart–Allmaras
Medium mesh $y^+ \approx 35$	Standard Wall function (SWF)	56.38	52.98	53.11	*55.21*[b]	*53.20*[b]	54.27	*53.25*[b]
	Non Equilibrium Wall Function	[a]	53.07	52.75			53.15	
	Scalable Wall Function	56.05	52.99	53.11			54.24	
Refined mesh $y^+ < 1$	Enhanced wall treatment (EWT)	52.60	52.66	51.83	52.13[c]	52.25[c]	52.31	52.88[d]
Difference between SWF and EWT[e] (%)		+6.71	+0.60	+2.41	+5.57	+1.78	+3.61	+0.70

[a] Difficulties in convergence: residuals for the continuity equation do not fall below 10^{-3}.
[b] Near wall treatment not needed because already implemented in the mathematical structure of the model. For this reason, only one value of the difference in static pressures is shown.
[c] Low-Re correction for the k–ω models activated in the viscous panel.
[d] The Spalart–Allmaras model, in its mathematical formulation, is a low Reynolds model and do not need any further specification for the wall treatment.
[e] Defined as $100 * [\Delta p_{SWF} - \Delta p_{EWT}]/\Delta p_{SWF}$.

interesting because of the presence of a short diverging part in the suction chamber, generating a small adverse pressure gradient. However, due to the (i) convergence issues with the k–ε Standard and (ii) the similar results compared to the other wall treatments, this wall treatment has not been considered. The Scalable-Wall-Function provides results very similar to the SWF without any considerable discrepancies.

- **Refined grid.** All the resulting pressure differences were smaller than the previous ones. However, the differences between the SWF approach and the EWT approach were negligible in most of the cases. The Spalart–Allmaras provide very similar results with the case of a coarse mesh, due to its low-Reynolds formulation.

As result of this analysis, the SWF approach is used in this study.

2.3. Boundary conditions and working fluid

At the inlet, mass flow conditions were imposed, whether at the outlet pressure conditions were set-up, accordingly to the experimental measurements (Table 2). Georgidias and Debonis [38] studied the influence on the turbulence boundary conditions for this case and, accordingly with their results we used a turbulence intensity I = 5% and 2% along with a turbulence viscosity ratio of μ_t/μ = 500 and μ_t/μ = 100, for the primary and the secondary flow respectively. The boundary conditions at the wall were set as no slip and adiabatic.

The working fluid is modeled as ideal gas and the properties (thermal conductivity, specific heat capacity and viscosity) of the air at atmospheric pressure and temperature of 25 °C were used. The modeling as ideal gas is mainly based on the working fluid (air) and the operating conditions (ambient temperature and pres-sure) adopted in the benchmark analyzed here. Furthermore, in the literature several studies adopt this approach in CFD analysis, such as Besagni et al. [4], Gagan et al. [29], Pianthong et al. [21], Sriveerakul et al.[39], Zhu and Jiang [26], and Zhu et al. [40].

2.4. Convergence criteria and computing time

To define the numerical simulations at a full convergence, the following criteria had to be satisfied at the same time:

(i) Decrease of the numerical residuals of six orders of magnitude.
(ii) Area-weighed-average value of the pressure at the inlets is constant.
(iii) Normalized difference of the mass flow rate between the boundaries was lower than 10^{-7}.

The complete analysis of convergence, including the coupling between the different turbulence models (using the SWF approach), can be found in the Appendix A and the results obtained are shown in Table 4.

3. CFD model result

The comparison between the numerical results and the experimental data concerns both global and local data. Considering the comparison of the global data, Table 5 summarizes the results for the pressure lift. Considering the comparison of the local data, velocity and temperature profiles at different nozzle distances are represented as a function of the dimensionless wall-distance $y^* = y_{value}/y_{wall}$ in Figs. 4–8. The CFD modeling resulted in a good performance prediction with the considered operating conditions.

3.1. Pressure lift

Table 5 summarizes the relative errors between the experimental pressure lift and the numerical results. The experimental pressure lift is obtained from Table 2 as the ratio between the secondary flow pressure and the mixing outlet pressure. The numerical pressure lift depends upon the resulting pressure at the inlet (the mixing outlet pressure is used as boundary condi-tion). For the Run 6 relative errors are below the 3%, for the RUN 7 below the 5.5%, for the RUN 9 and 10 below 15%. In particular, the relative errors considering the RUN 9 are slightly lower than the RUN 10. This is probably related to the increased entrainment ratio for the different RUNs (Table 2). Comparing the turbulence models, the k–ω SST and the Spalart–Allmaras showed, for every case, good performance. It is worth noting that the present valida-tion concerns a global parameter and not local data. Despite the correct evaluation of the pressure loss may ensure that the mixing

Table 4
Turbulence models: convergence analysis.

	k–ε Standard	k–ε Realizable	k–ε RNG	k–ω Standard	k–ω SST	RSM	Spalart–Allmaras
Nr. Iterations	1	0.945	0.926	1.013	0.947	0.980	0.934
Δ[*Nr. Iterations*] (%)[a]	–	−5.49	−7.35	1.32	−5.30	−1.98	−6.65
$CPU_{Iteration\ time}$	1	1.024	1.195	1.039	1.061	1.174	0.998
$\Delta[CPU_{Iteration\ time}]$ (%)[a]	–	2.37	19.46	3.89	6.09	17.43	−0.17
$CPU_{Simulation\ time}$	1	0.967	1.107	1.053	1.005	1.151	0.932
$\Delta[CPU_{Simulation\ time}]$ (%)[a]	–	−3.25	10.68	5.26	0.47	15.10	−6.81

[a] Evaluated as $100 * [k\text{–}\varepsilon_{value} - \text{model}_{value}]/k\text{–}\varepsilon_{value}$.

Table 5
Pressure lift: relative errors between experimental and numerical results.

	Spalart–Allmaras	k–ε Standard	k–ε RNG	k–ε Realizable	k–ω Standard	k–ω SST	RSM
RUN 6	1.07	1.81	0.77	1.72	2.32	1.77	2.84
RUN 7	3.88	4.71	3.62	4.68	5.37	4.68	5.55
RUN 9	11.04	12.16	11.05	11.79	12.47	11.63	12.39
RUN 10	11.91	13.00	12.03	12.55	13.29	12.40	13.10

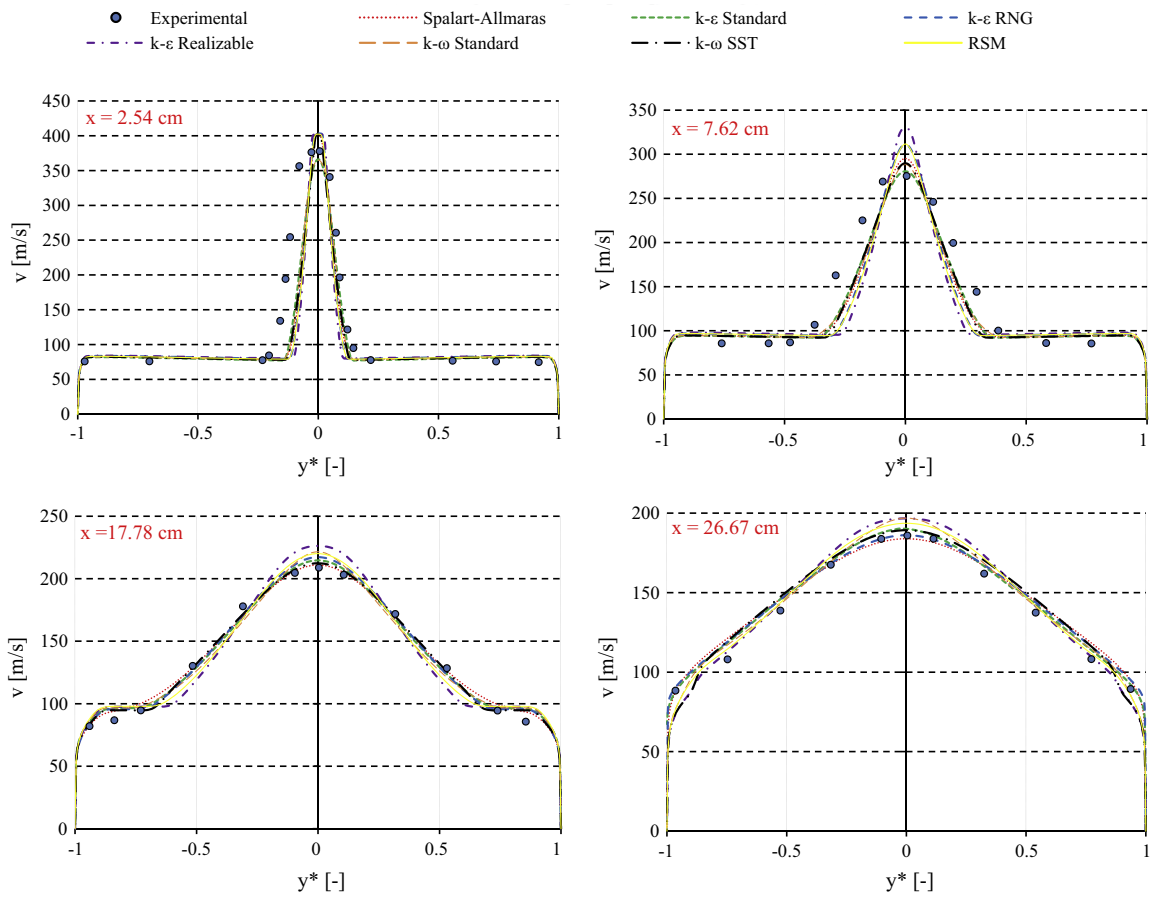

Fig. 4. Velocity profiles (run 6).

losses and friction losses are estimated correctly, a fully validated approach rely on a local comparison with the experimental data. This is discussed in the following sections.

3.2. Flow field

The comparison between the CFD predictions and the experimental results are showed in Figs. 4–7 (RUN 6–9). There is no remarkable difference between the different operating conditions tested, proving that the modeling approach is suitable for studying different operating conditions. Concerning centerline data, near nozzle exit the k–ω and k–ε models underestimate the experimental values (the relative error for the centerline data is −3% to −6%) whereas k–ε RNG, k–ε Realizable and linear RSM overestimate (the relative error for the centerline data is 6–15%, 6–13% and 6–10%, respectively). The k–ω SST and Spalart–Allmaras models achieved higher performance (the relative error for the centerline data is +2–6%). Downstream the k–ω SST, Spalart–Allmaras, k–ε and k–ε RNG, models properly represented the flow field, whereas other models overestimated the experimental values: the k–ε Realizable and k–ω by 3–6% and the linear RSM by 1–4%. Concerning the near-wall data, all the models are able to predict these values quite well both near ejector nozzle and downstream. This confirms the suitability of the near-wall-treatment employed.

Near the ejector nozzle, all the models show some limits reproducing the flow in the central part of the section, with the initial growth region of the jet characterized by higher errors and the under prediction of the jet spreading rate. In the central region the RANS approach, including the more advanced models, has some weaknesses and the average error can increase. At the same time the experimental measurements suffer of lack of accuracy in the center region, as explained by the authors of the experimental campaign [31]. The lateral values were quite well predicted and this suggests that the observed deficiency is correlated to the turbulent shear stress and the jet-spreading rate. Out of the jet core the mixing rate becomes too high. The literature suggests that this behavior is due to the modeling of the turbulent diffusion [41]. Another source of error is the uncertainty of the turbulence boundary conditions [42]. Finally, it is worth noting that each RANS model was developed for particular benchmark. In future studies, the model prediction could be improved by modification of the model constants (i.e., the production and dissipation terms), a

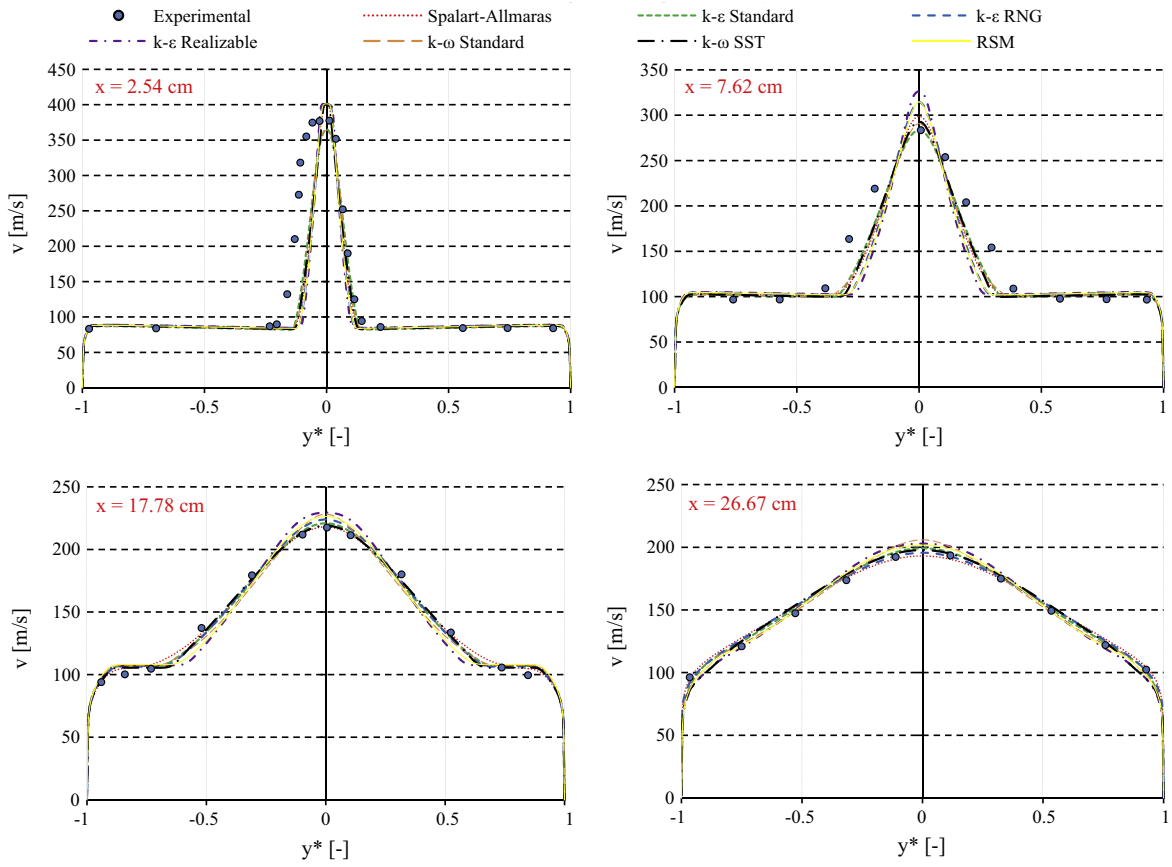

Fig. 5. Velocity profiles (run 7).

correction in the model diffusion coefficients and/or the inclusion of cross-diffusion contributions.

3.3. Thermal field

The comparison between the CFD predictions and the experimental results has been shown in Fig. 8 (RUN 9). All the models analyzed here were not able to fit experimental data near nozzle and the centerline data were overestimated (the relative error for the centerline data is 1–3%). Far from the nozzle exit, all the models, except for the k–ω, fit the experimental data fairly well. The Spalart–Allmaras shown excellent results, while k–ω SST, even if it is under predicting later values, performed quite well. A possible reason of these discrepancies may lie in the presence of a constant value for the turbulent Prandtl number [43]. The literature suggested the use of a multi-zonal approach or some more sophisticated approaches for solving this issue [44,45], but the implementation of these methods is far beyond the scope of this paper.

3.4. Comparison with the literature

The influence of RANS turbulence modeling over the results is matter of intensive study in the literature. Bartosiewicz et al.[34] found that the k–ω SST and k–ε RNG models well predict the line of pressure recovery and the shock phase. Bouhanguel et al. [35] showed that the results are strongly dependent on the turbulence models and none of the model tested was able to capture the shock reflection at the nozzle exit. The Realizable k–ε was suggested by Dvorak and Vit [36]. Kolar and Dvorak [37] suggested the k–ω SST for the prediction of shock waves and boundary layer separations, even if this model over-predicted the shear stress. Gagan et al. [29] suggested the k–ε Standard. The k–ε RNG, linear RSM and k–ω do not predict vortex downstream nozzle, whereas the k–ω SST and the Realizable k–ε underpredict the vortex scale.

4. Lumped Parameter Model (LPM)

A steady-state lumped parameter model for a convergent nozzle ejector is presented. This model will be integrated with the ejector efficiency maps presented in next paragraph, creating the Integrated LPM-CFD model. The purpose of this approach is to evaluate for a fixed geometry, and for both on-design and off-design operating conditions, the entrainment ratio.

4.1. On-design and Off-design operation conditions

Before present the LPM, some details are given concerning the ejector working conditions. A convergent nozzle ejector may work in three different modes:

1. **critical mode.** The primary flow is choked and the secondary mass flow rate is constant;
2. **subcritical mode.** The primary flow is not choked and there is a high dependence of the secondary mass flow rate on the value of the exit pressure;
3. **malfunction mode.** The primary flow reversed in the suction chamber.

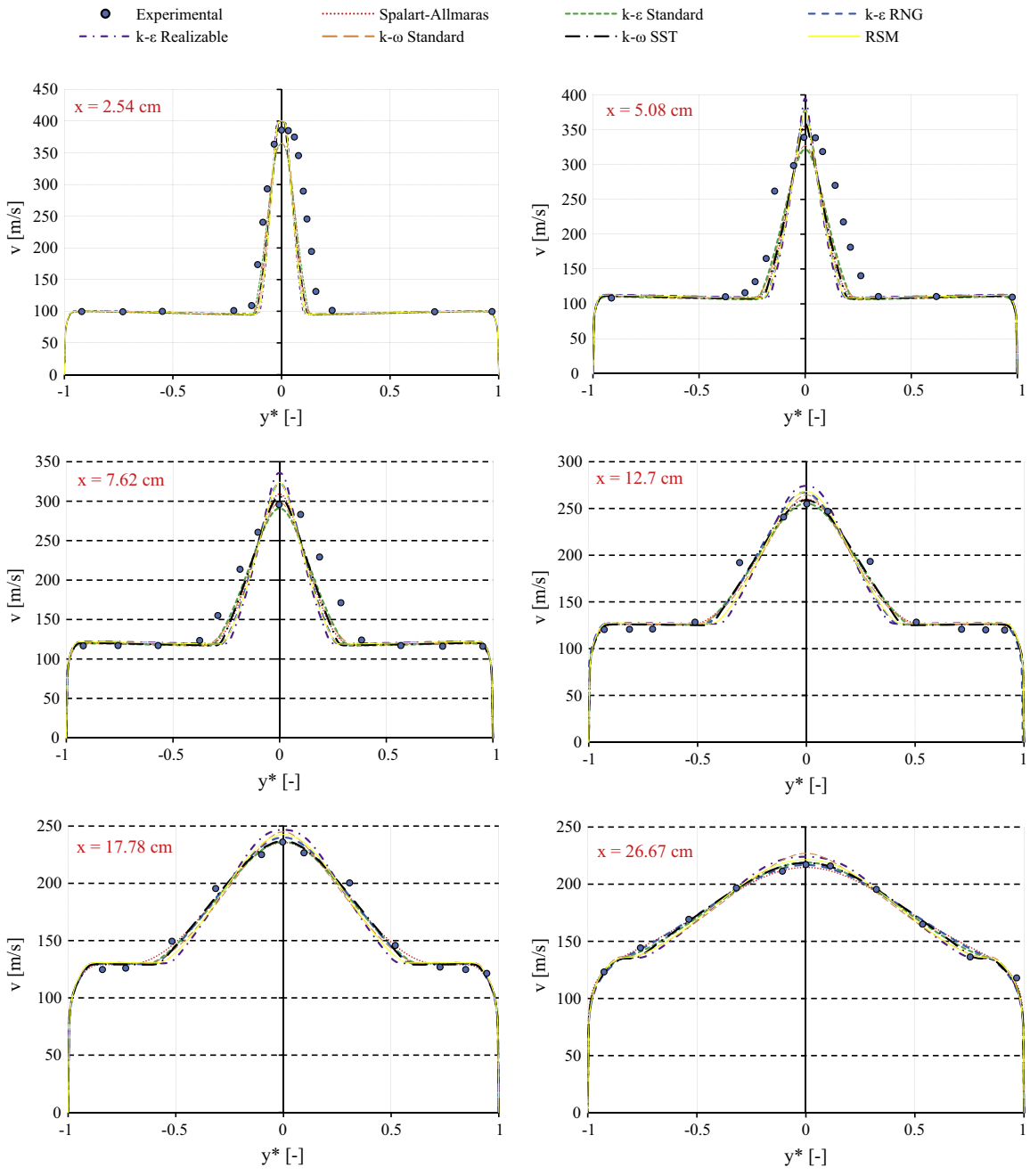

Fig. 6. Velocity profiles (run 9).

In this paper, we refer to On-design operation when the ejector works in the critical mode and the primary flow is chocked. When the primary flow is not chocked we refer to Off-design operating condition. The ejector may work in Off-design operating condition during change of load or start-up. Therefore, the correct evaluation of both On-design and Off-design operating conditions are of great importance in the modeling of the whole ejector based systems. In order to take into account the Off-design operating condition, the mathematical structure of the LPM should be suitable (Section 4.3). However, as discussed in Section 6.2, the appropriate mathematical structure of the LPM is not enough to ensure the correct modeling of the Off-design condition. Therefore, variable ejector efficiencies should be used for taking into account the local phenomena and the ILPM-CFD model is needed. This is discussed in Sections 5 and 6.

4.2. Model hypothesis

The model is based on four main assumptions:

(I) adiabatic walls;
(II) the working fluids are treated as ideal gases;
(III) uniform velocity and thermodynamic conditions at each cross-section;
(IV) primary and secondary flows have total (stagnant) conditions at inlets.

Those assumptions are common to the LPMs found in the literature. The reader should also refer to the review of He et al. [3], concerning the mathematical models till the 2009, and to the paper of Besagni et al. [16], concerning the comparison of five different

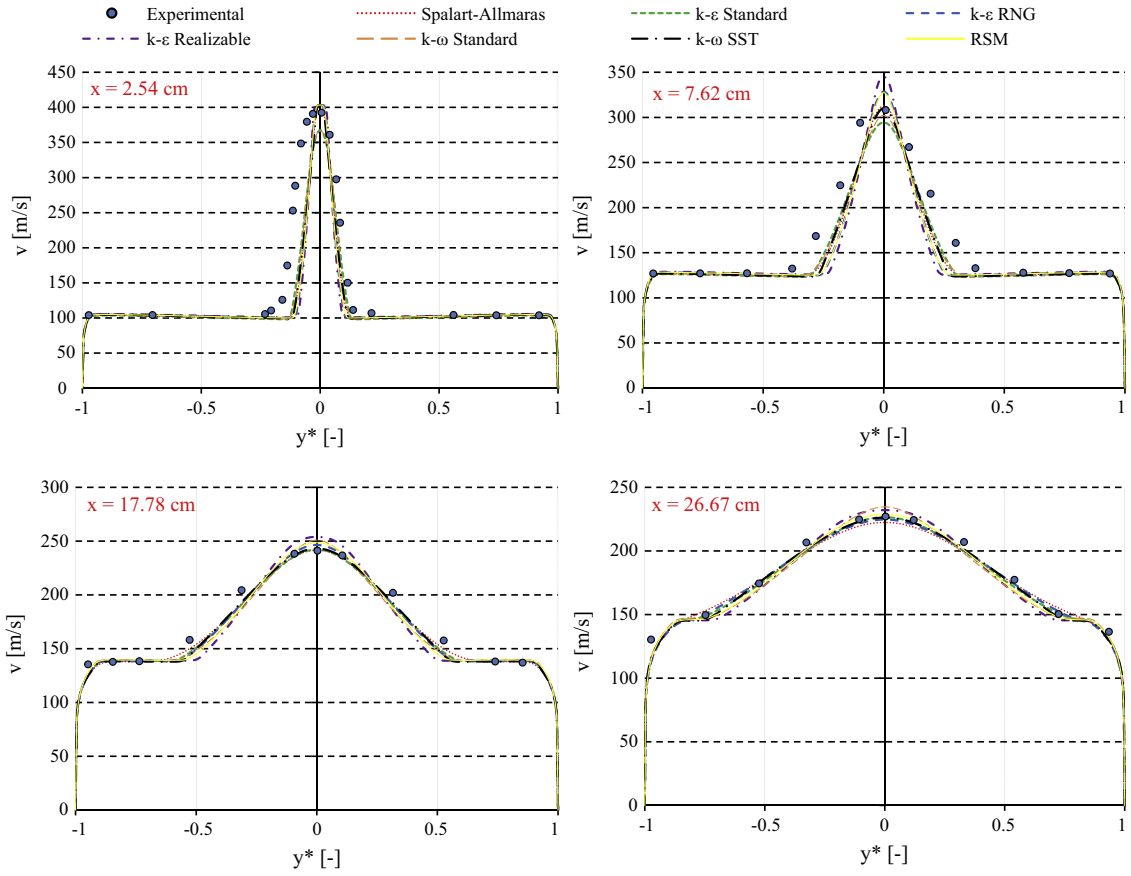

Fig. 7. Velocity profiles (run 10).

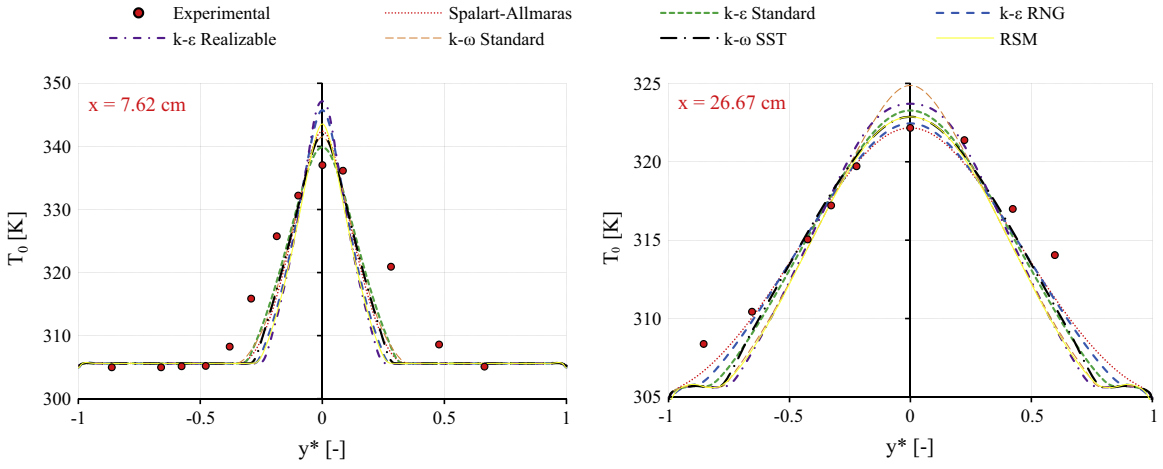

Fig. 8. Total temperature profiles (run 9).

LPMs. The above-mentioned assumptions are, therefore, coherent with the typical assumptions made while developing LPMs. It is important to notice that, in the perspective coupling of LPM and the CFD approach, the same thermodynamic properties should be used (i.e., the hypothesis of ideal gas).

The model provides as output the entrainment ratio $\omega = \dot{m}_s/\dot{m}_p$ using as input ejector geometry, $p_{p,in}$, $p_{s,in}$ (a pressure-inlet lumped parameter model), $T_{p,in}$, $T_{s,in}$. An additional information is needed for closing the problem. In this work, $M_{s,t}$ was used because it is known from CFD simulations. This data can be seen as the expansion ratio in the suction chamber β (with $\beta = p_{s,in}/p_{s,t}$). The accuracy of obtaining $M_{s,t}$ by using the CFD model is ensured by the validation numerical approach. For the validated cases the agreement between the experimental and numerical results was good especially for the lateral data (refer to Section 3.1.2). $M_{s,t}$ refers to the suction chamber exit which concerns the lateral values in the Figs. 4–7, which are well predicted by the CFD approach. The CFD approach is, therefore, suitable for the prediction of the flow field of the secondary flow and, in particular, $M_{s,t}$. Other choices can be (i) $\dot{m}_s$, (ii) p_{out} or (iii) a hypothesis on velocity

distribution inside the ejector [5]. The present model can be easily modified according to the chosen closure.

4.3. Model structure

This model is structured to solve firstly the suction chamber, secondly the primary nozzle and finally the mixing chamber. The interested reader may also refer to the paper of Zhu et al. [5] concerning the mathematical modeling of a convergent nozzle ejector. It is worth noting that the present LPM differs from the models presented in the literature for the solving procedure (the reader should refer, for example, the models of Huang et al. [46] or the model of Zhu et al. [5], to the model comparison of Besagni et al. [16] and to the review of He et al. [3]). The main difference from the literature models is that, in the present case, the first compo-nent solved is the suction chamber and not the primary nozzle.

4.3.1. Suction chamber

In this study, CFD simulations have been used for obtaining $M_{s,t}$. Given $M_{s,t}$, $\dot{m}_s$ can be evaluated as follows:

$$\dot{m}_s = M_{s,t} p_s A_s \sqrt{\frac{\gamma \eta_s}{R * T_s}\left(1 + \frac{\gamma - 1}{2} M_{s,t}^2\right)^{\frac{\gamma-1}{\gamma+1}}} \tag{1}$$

where isentropic efficiency η_s takes into account friction losses and irreversibility. η_s is the ratio between the static enthalpy drop across the suction chamber and the isentropic drop from the same initial conditions to the final pressure:

$$\eta_s = \frac{h_{s,in} - h_{s,t}}{h_{s,in} - h_{s,t,is}} \tag{2}$$

Static temperature, pressure and velocity at suction chamber exit can be evaluated accordingly:

$$T_{s,t} = \frac{T_{s,in}}{1 + \frac{\gamma-1}{2}\eta_s M_{s,t}^2} \tag{3}$$

$$p_{s,t} = \frac{p_{s,in}}{\left(1 + \frac{\gamma-1}{2}\eta_s M_{s,t}^2\right)^{\frac{\gamma}{\gamma-1}}} \tag{4}$$

$$v_{s,out} = \frac{\dot{m}_s}{\rho_{s,t} A_s} = R * T_{s,t} \frac{\dot{m}_s}{p_{s,t} A_s} \tag{5}$$

4.3.2. Primary nozzle

In a convergent nozzle, the flow can be either subsonic or sonic. The flow is subsonic when the pressure ratio is lower than:

$$v_{cr} = \left(\frac{p_{s,t}}{p_{p,in}}\right)_{cr} = \left(\frac{2}{\gamma + 1}\right)^{\frac{\gamma}{\gamma-1}} \tag{6}$$

Both $M_{p,t}$ and $\dot{m}_p$ can be obtained from isentropic relations. If primary flow is not chocked, $p_{p,t}$ is equal to $p_{s,t}$, otherwise it is not influenced by secondary flow. In the following expressions η_p is used for considering friction losses and irreversibility:

$$\eta_p = \frac{h_{p,in} - h_{p,t}}{h_{p,in} - h_{p,t,is}} \tag{7}$$

for sonic primary flow ($p_{p,in} \geqslant p_{s,t}/v_{cr}$):

$$\dot{m}_p = p_{p,in} A_{p,t} \sqrt{\frac{\eta_p \gamma}{R * T_{p,in}}\left(\frac{2}{\gamma + 1}\right)^{\frac{\gamma+1}{\gamma-1}}} \tag{8}$$

$$M_{p,t} = 1 \tag{9}$$

$$p_{p,t} = \frac{p_{p,in}}{\left(1 + \frac{\gamma-1}{2}\eta_p M_{p,t}^2\right)^{\frac{\gamma}{\gamma-1}}} \tag{10}$$

for sub-sonic primary flow ($p_{p,in} < p_{s,t}/v_{cr}$):

$$\dot{m}_p = A_{p,t} p_{p,in} \sqrt{\frac{2\eta_p \gamma\left[\left(\frac{p_{s,t}}{p_{p,in}}\right)^{\frac{2}{\gamma}} - \left(\frac{p_{s,t}}{p_{p,in}}\right)^{\frac{1+\gamma}{\gamma}}\right]}{R * T_{p,in}(\gamma - 1)}} \tag{11}$$

$$M_{p,t} = \sqrt{2\frac{\left[1 - \left(\frac{p_{s,t}}{p_{p,in}}\right)^{\frac{\gamma-1}{\gamma}}\right]}{(\gamma - 1)}} \tag{12}$$

$$p_{p,t} = p_{s,t} \tag{13}$$

4.3.3. Mixing zone

The evaluation of the mixing process is simpler than constant pressure or constant area models: the hypothesis of aerodynamic throat or premixing zone is not used. The behavior of the ejector is described by efficiency maps introduced in the balance equations. The balance equations are written from considering the control volume between the nozzle throat plane and the mixing zone outlet:

$$\dot{m}_p + \dot{m}_s = \frac{p_{out} v_{out} A_{out}}{R * T_{out}} \tag{14}$$

$$\eta_{mix}\left[(\dot{m}_p v_{p,t} + p_{p,t} A_{p,t}) + (\dot{m}_s v_{s,t} + p_{s,t} A_{s,t})\right] = (\dot{m}_s + \dot{m}_p) v_{out} + p_{out} A_{out} \tag{15}$$

$$\dot{m}_p \quad c_{p,p} T_{p,out} + \frac{v_{p,t}^2}{2}\Bigg) + \dot{m}_s \quad c_{p,s} T_{s,t} + \frac{v_{s,t}^2}{2}\Bigg) = (\dot{m}_s + \dot{m}_p)\left(c_{p,out} T_{out} + \frac{v_{out}^2}{2}\right) \tag{16}$$

From this system p_{out}, T_{out} and v_{out} can be obtained. Mixing efficiency η_{mix} is defined from above equations:

$$\eta_{mix} = \frac{(\dot{m}_s + \dot{m}_p) v_{out} + p_{out} A_{out}}{(\dot{m}_p v_{p,t} + p_{p,t} A_{p,t}) + (\dot{m}_s v_{s,t} + p_{s,t} A_{s,t})} \tag{17}$$

In next paragraph ejector component efficiencies will be evaluated and discussed. In Section 6, the integration of ejector efficiency maps in this model, thus creating the Integrated LPM-CFD model.

5. Ejector component efficiencies: CFD evaluation

5.1. Ejector efficiency evaluation procedure

The ejector efficiencies have been obtained by using the numerical method and geometrical discretization described for the CFD approach. The validation process ensures the reliability of the efficiency evaluated in this section. The boundary conditions have been varied in order to investigate different operating conditions of a convergent nozzle ejector: from a subsonic flow to under-expanded jets. The subsonic flow field concerns a flow field without choking phenomena and/or zone of the domain with Mach number equal or above 1. The under expanded flow fields concerns the under-expanded primary flow: at the nozzle's exit plane, the primary flow pressure is higher than that of the secondary flow and the so called 'shock train' (a succession of oblique and/or nor-mal shock waves) occurs. When considering the flow fields in a rectangular shape ejector, the interested reader may also refer to the study of Little et al. [1], Hsia et al. [47] and Koite et al. [48].

The information from each solution have been used to evaluate the ejector component efficiencies from Eqs. (2, 7 and 17) and by using FluidProp [49] for the thermodynamic properties. In all the conditions analyzed, the secondary flow does not reach full double choking condition. This occurs for two reasons. Firstly, the mixing chamber diameter is larger if compared to common ejectors [3] and, therefore, the aero-dynamic throat is large. Secondly, a subsonic ejector has less entrainment effect if compared to a supersonic ejector [5]. Indeed, primary flow may reach only sonic condition at nozzle outlet and the primary flow cannot accelerate

the entrained flow like in a supersonic ejector. As consequence of the absence of double choking, ejector efficiencies are computed considering inlet and outlet parameters, such as discussed by Besagni et al. [20], who proposed the pressure ratios:

$$\varphi_p = p_{0p,in}/p_{out} \tag{18}$$

$$\varphi_s = p_{0s,in}/p_{out} \tag{19}$$

In particular, the η_p mostly depends upon φ_p, η_s upon φ_s and η_{mix} is a function of both φ_p and φ_s (Figs. 9 and 10):

- η_p = 0.5, for subsonic flow, and increases, reaching a constant value of η_p = 0.95, for under-expanded jet. η_p, then, remains constant because of choking preventing downstream conditions (p_{out}) to travel upstream (Fig. 10).
- η_p ranges from $\eta_s \approx 0.1$ till a maximum value $\eta_s \approx 0.64$–0.65. The non-optimized geometry causes the low values: suction chamber has a little diverging part, causing an adverse pressure gradient (which is more critical for low $p_{s,in}$).
- In a subsonic flow η_{mic} = 0.60–0.70, and increases to η_{mix} = 0.75–0.80 for under-expanded jet, till η_p = 0.85–0.95 for highly under-expanded (Fig. 10). It is known from the literature that over expanded jets have higher mixing rates [50] due to shock-boundary layer interactions that disturbs the mixing layer [51]. This effect was also observed in a two dimensional supersonic ejector where the length of mixing was found to be reduced by about 50% [52].

5.2. Ejector efficiencies maps

Efficiency maps have been obtained by using regression equations and are summarized in Table 6. The parameters in the regression equations have uncertainty and were chosen as the best compromise between good approximation and the equation complexity. Proposed maps are able to predict η_p, η_s and η_{mix} CFD values with a mean error of 0.69%, 2.86% and 0.71%, respec-tively. The mean error is defined as the average of the relative errors of each point compared. The empirical correlations were obtained and should be used in the following range:

$$1.07 < \varphi_p < 41.96 \tag{20}$$

$$0.91 < \varphi_s < 2.58 \tag{21}$$

The correlations and related maps are built by running 44 different simulations covering a large range for the primary and secondary flow. The simulated cases are represented as bullet points the efficiency maps presented in Fig. 9. The validated numerical approach reported in Section 2 is used for the simulations guarantying the reliability of the correlations carried out.

The efficiency maps take into account the variation of the operating conditions, but efficiency values depend also upon ejector geometry and working fluid. Further studies are needed for inferring considerations for a circular shape ejector. For example, Besagni et al. [53] have studied an axi-symmetric convergent-nozzle ejector and similar ejector efficiency maps have been reported. The change of working fluid leads to a change in fluid properties (i.e., molecular mass, viscosity and density) and a change in the Reynolds number, the sonic velocity and the friction losses. The maps presented here could be used for different work-ing fluids if the similitude is respected. The detailed explanation of the similitude analysis for the case of an ejector was presented by Brunner et al. [54]. Given the non-dimensional analysis and the flow fields investigated, in the present case the similitude is ensured under the following conditions: equality of *Re*, *M*, γ and geometry similitude. In particular, the range of the simulation carried out in this study is as follows:

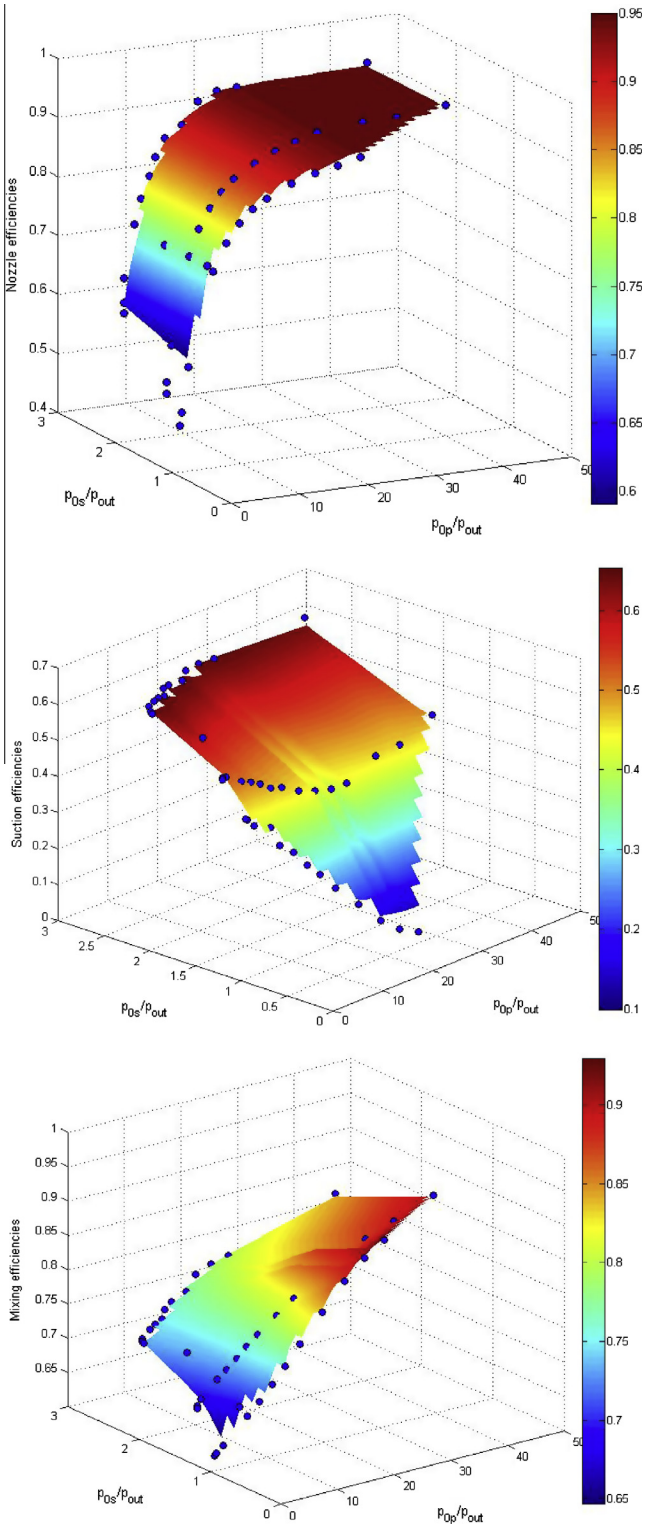

Fig. 9. Ejector component efficiencies (efficiency maps).

$$0.147 < M_t < 1 \tag{22}$$

$$3725 < Re_t < 10152 \tag{23}$$

Under the hypothesis of ideal gas, the equality of γ means that these maps are for diatomic gases only. Recently, this has been discussed and demonstrated for the case of Hydrogen as working fluid for an axi-symmetric convergent nozzle ejector [53].

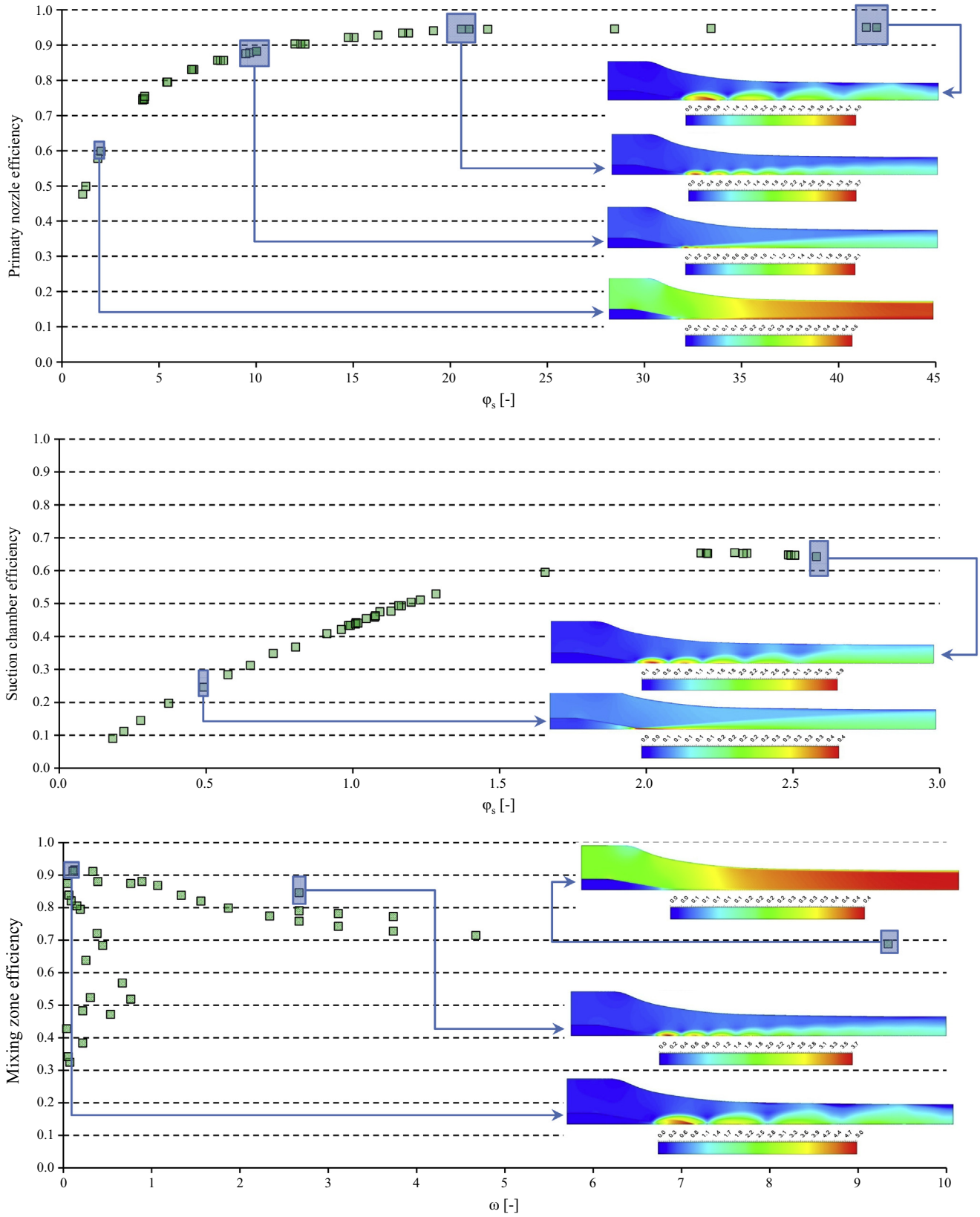

Fig. 10. Ejector efficiencies: relation with the flow field (Mach contour).

Table 6
Ejector efficiencies regressing equations.

Efficiency	Regressing equation	R^2	Mean error (%)
η_p	$0.9391e^{0.000308\varphi_p} - 0.5029e^{-0.2176\varphi_p}$	0.9968	0.69
η_s	$-0.1234\varphi_s^2 + 0.5699\varphi_s - 0.0053$	0.9993	2.85
η_{mix}	$0.6417 + 0.02571\varphi_p - 0.0569\varphi_s - 0.0005567\varphi_p^2 - 0.007734_{11}\varphi_p\varphi_s$ $+0.06695\varphi_s^2 + 0.000003393\varphi_p^3 + 0.0001373\varphi_p^2\varphi_s - 0.00002624\varphi_p\varphi_s^2 - 0.01243\varphi_s^3$	0.9884	0.71

Table 7
Ejector component efficiencies used in the literature.

Ref.	η_p	η_s	η_{mix}	η_d
Eames et al. [56]	0.85		0.95	0.85
Sun [57]	0.85			0.85
Grazzini and Mariani [58]	0.90		1.0	0.85
Aly et al. [15]	0.90		0.95	0.90
Huang et al. [46]	0.95	0.85	0.80–0.84	
Huang and Chang [59]		0.85		
Sun [60]	0.85			0.85
Rogdakis and Alexis [61]	0.80		0.80	0.80
Cizungu et al. [62] Alexis	0.95	0.95		0.85
and Rogdakis [63]	0.90		0.80	0.80
Selvaraju and Mani [64]	0.95	0.95		0.85
Yapici and Ersoy [65]	0.85	0.85		0.85
Li and Groll [66]	0.90	0.90		0.80
Yu et al. [67]	0.85		0.95	0.85
Deng et al. [68]	0.70			0.80
Zhu et al. [10]	0.90–0.95			
Godefroy et al. [69]	0.80	0.95	0.935	0.80
Yu and Li [70]	0.90		0.85	0.85
Yu et al. [71]	0.90		0.85	0.85
Sarkar [72]	0.80	0.80		0.75
Elbel and Hrnjak [73] Zhu	0.80	0.80		0.80
and Li [12] Fangtian and	0.72–0.90			
Yitai [74] Cardemil and	0.90	0.90		0.80
Colle [75] Liu et al. [76]	0.85–0.95	0.95	0.75–0.95	0.95
Vereda et al. [77] Manjili	0.50–0.93	0.37–0.90	0.50–1.00	
and Yavari [78] Liu and	0.85	0.85	0.90	0.80
Groll [18]	0.70	0.70	0.95	0.80
Varga et al. [19]	0.50–0.93	0.37–0.90	0.50–1.00	
Chen et al. [17] Kasperski	0.92–0.95	0.84–0.90	0.65–0.98	0.50–0.89
and Gil [79] Besagni et al.	0.70–0.98		0.70–0.98	0.72–0.98
[16] Goodarzi et al. [80]	0.95	0.85	0.80–0.84	
	0.95	0.95	0.85 0.95	0.9
	0.80			0.80

5.3. Comparison with the literature

In this study, η_p, η_s and η_{mix} range from 0.50 to 0.95, from 0.10 to 0.65, and 0.65 to 0.90, respectively: this range is larger if compared to the constant values commonly used in the literature and is comparable with other studies focused on ejector efficiencies [18,19]. A summary of the ejector efficiency values used in the previous literature is presented in Table 7. The interested reader may also refer to the review of Liu [14].

Other works focused on ejector component efficiencies are the studies of Liu and Groll [18], Varga et al. [19] and Besagni et al. [53]. Liu and Groll [18] investigated a two-phase subsonic ejector, Varga et al. [19] a single-phase supersonic ejector and Besagni et al. [53] an axialy-symmetrical convergent nozzle. In the following a comparison of the value if provided:

- Varga et al. [19] reported η_p independent from outlet conditions (the motive nozzle was chocked). The range of η_p found by Liu and Groll [18] agrees with our results. Besagni et al. [53] found a similar shape of the nozzles ejector efficiency.
- The shape of the suction chamber in the previous studies is quite different and the results of Varga et al. [19] (η_S is nearly constant in critical condition and drops in subcritical operation) confirm our results for the constant value of η_p. This trend was also found by Liu and Groll [18].
- The range of variation of η_{mix} in our study is similar to the one by Varga et al. [19], Liu and Groll [18] and Besagni et al. [53]. It is worth noting that our efficiency definition takes into account also the pressure terms, such as [18]. Banasiak et al. [55] found that efficiencies evaluated without the pressure contribution exceeded 100% because of the actual expansion instead of the expected compression in that section.

A summary of the efficiency maps presented in the literature [17,18,53] have been summarized in Table 8. The reader should refer to the original references for a detailed discussion concerning those efficiency maps, their limitation and range of applicability. It is worth noting that the maps presented by Chen et al. [17] have been obtained by processing the experimental data obtained by Huang et al. [46] and not by an ad-hoc analysis focused on ejector component efficiencies. Fig. 11 presents, for the sake of clearness, the efficiency maps proposed by Liu and Groll [18], which depends also on geometrical parameters.

6. Integrated LMP-CFD model: Validation and evaluation

Herein, the Integrated LPM-CFD model is presented, discussed, validated and compared with LPM with Constant Efficiencies (LPM-CE models).

6.1. Integrated LPM-CFD (ILPM-CFD) model building

The CFD model presented in Section 3 and the LPM presented in Section 4 belong to different modeling techniques. These modeling techniques can be coupled by using ejector efficiency maps, such as those presented in Section 5.1. In this framework, the ejector efficiencies are a way to taking into account local phenomena in LPMs. The usage of ejector efficiency maps in the LPM model was possible because (i) efficiencies definitions were coherent in CFD and LPM models and (ii) the CFD and LPM models have both been built using a working fluid with the same thermodynamic properties.

6.2. ILPM-CFD Solving procedure

Herein, the iterative solving procedure (Fig. 12) for the ILPM-CFD model is presented and discussed. Starting from $p_{p,in}$, $p_{s,in}$, $T_{p,in}$, $T_{s,in}$, $M_{s,t}$ suction chamber is solved by using Eqs. (1–5). Then, the flow condition through primary nozzle is evaluated (6) and primary nozzle is solved by using either Eqs. (7–10) or Eqs. (11–13) for the case of sonic or subsonic flow, respectively. Then mixing zone is solved by Eqs. (14–17) and ejector efficiencies are updated. At last, a check is performed over both (i) efficiency values and every (ii) model outputs. Convergence is supposed to be reached when the residuals are less than 10^{-6}. This level of convergence is reached in about 10 iterations. A relaxation factor for ejector

Table 8
Ejector efficiency maps (correlations) from the literature.

Reference	Working fluid	Ejector component	Efficiency formulation
Besagni et al. [53]	Air	Primary nozzle	$0.969e^{0.00043\left(\frac{p_p}{p_s}\right)} - 6.214e^{-2.93\left(\frac{p_p}{p_s}\right)}$
Besagni et al. [53]	Air	Suction chamber	$0.864e^{0.0832m_{s,ad}} - 1.083e^{-16.41m_{s,ad}}$
Besagni et al. [53]	Air	Mixing chamber	$0.5761 + 0.01995\left(\frac{p_p}{p_s}\right) - 0.0275m_{s,ad} - 0.0008652\left(\frac{p_p}{p_s}\right)^2 + 0.02206\left(\frac{p_p}{p_s}\right)m_{s,ad} - 0.08955m_{s,ad}^2 + 0.000142\left(\frac{p_p}{p_s}\right)^3$ $-0.002835\left(\frac{p_p}{p_s}\right)^2 m_{s,ad} + 0.1431\left(\frac{p_p}{p_s}\right)m_{s,ad}^2 - 3.503m_{s,ad}^3 - 0.000005837\left(\frac{p_p}{p_s}\right)^4 - 0.00008721\left(\frac{p_p}{p_s}\right)^3 m_{s,ad}$ $+0.009375\left(\frac{p_p}{p_s}\right)^2 m_{s,ad}^2 + 0.08513\left(\frac{p_p}{p_s}\right)m_{s,ad}^3 - 5.059m_{s,ad}^4$
Besagni et al. [53]	Air	Diffuser	$0.9655 + 0.2338\left(\frac{p_p}{p_s}\right) - 11.17m_{s,ad} - 0.1215\left(\frac{p_p}{p_s}\right)^2 + 1.583\left(\frac{p_p}{p_s}\right)m_{s,ad} + 67.38m_{s,ad}^2 + 0.01291\left(\frac{p_p}{p_s}\right)^3$ $-0.02569\left(\frac{p_p}{p_s}\right)^2 m_{s,ad} - 4.124\left(\frac{p_p}{p_s}\right)m_{s,ad}^2 - 259.4m_{s,ad}^3 - 0.0003611\left(\frac{p_p}{p_s}\right)^4 - 0.0164\left(\frac{p_p}{p_s}\right)^3 m_{s,ad}$ $+0.6397\left(\frac{p_p}{p_s}\right)^2 m_{s,ad}^2 - 8.234\left(\frac{p_p}{p_s}\right)m_{s,ad}^3 - 437.1m_{s,ad}^4$
Besagni et al. [53]	Hydrogen	Primary nozzle	$0.967e^{0.002068\left(\frac{p_p}{p_s}\right)} - 6.311e^{-3.005\left(\frac{p_p}{p_s}\right)}$
Besagni et al. [53]	Hydrogen	Suction chamber	$5.765e^{-3.263m_{s,ad}} - 5.78e^{-4.989m_{s,ad}}$
Besagni et al. [53]	Hydrogen	Mixing chamber	$5.7565 + 0.01836\left(\frac{p_p}{p_s}\right) + 0.06731m_{s,ad} - 0.0015\left(\frac{p_p}{p_s}\right)^2 - 0.01775\left(\frac{p_p}{p_s}\right)m_{s,ad} + 0.381m_{s,ad}^2$
Besagni et al. [53]	Hydrogen	Diffuser	$5.653 - 7.721\left(\frac{p_p}{p_s}\right) - 24.47m_{s,ad} + 3.87\left(\frac{p_p}{p_s}\right)^2 + 9.972\left(\frac{p_p}{p_s}\right)m_{s,ad} + 121.2m_{s,ad}^2 - 0.832\left(\frac{p_p}{p_s}\right)^3$ $-1.834\left(\frac{p_p}{p_s}\right)^2 m_{s,ad} - 22.86\left(\frac{p_p}{p_s}\right)m_{s,ad}^2 - 308.7m_{s,ad}^3 + 0.064\left(\frac{p_p}{p_s}\right)^4 + 0.155\left(\frac{p_p}{p_s}\right)^3 m_{s,ad} - 0.17\left(\frac{p_p}{p_s}\right)^2 m_{s,ad}^2 + 60.05\left(\frac{p_p}{p_s}\right)m_{s,ad}^3$
Liu and Groll [18]	Air	Primary nozzle	$-36.137 - 4.160\left(\frac{p_p}{p_s}\right) + 1.161\left(\frac{p_p}{p_s}\right)^2 - 0.106\left(\frac{p_p}{p_s}\right)^3 + 212.320\left(\frac{d_{mix}}{d_t}\right) - 355.359\left(\frac{d_{mix}}{d_t}\right)^2 + 196.035\left(\frac{d_{mix}}{d_t}\right)^3$
Liu and Groll [18]	Air	Suction chamber	$-3173.171 - 934.12\left(\frac{p_p}{p_s}\right) + 314.471\left(\frac{p_p}{p_s}\right)^2 + 79.521\left(\frac{p_p}{p_s}\right)^3 - 12.222\left(\frac{p_p}{p_s}\right)^4 + 0.814\left(\frac{p_p}{p_s}\right)^5 + 694,222.1\omega$ $+2,956,145\omega^2 + 7,950,453\omega^3 - 114,327,270\omega^4 + 6,689,155\omega^5 - 649,905.1Z + 2,647,000Z^2$ $-6,885,025Z^3 + 9,627,161Z^4 - 5,490,126Z^5$
Liu and Groll [18]	Air	Mixing chamber	$-6,869.077 + 19,308.18Z' - 18,089.31Z'^2 + 5649.417Z'^3$
Chen et al. [17]	R141b	Primary nozzle	0.95 (constant value)
Chen et al. [17]	R141b	Mixing chamber	$7.7837 + 0.1611\left(\frac{p_p}{p_{out}}\right)^2 - 2.6404\left(\frac{p_p}{p_{out}}\right) + 0.1924\left(\frac{p_{out}}{p_s}\right)^2 - 2.4919\left(\frac{p_{out}}{p_s}\right) - 0.0123\left(\frac{p_p}{p_s}\right)^2 + 0.6634\left(\frac{p_p}{p_s}\right)$ $-0.0172\left(\frac{A_{mix}}{A_t}\right)^2 + 0.3479\left(\frac{A_{mix}}{A_t}\right) + 0.1611\omega^2 + 0.3767\omega$
Chen et al. [17]	R141b	Diffuser	$2.3109 + 0.1682\left(\frac{p_p}{p_{out}}\right) - 0.0223\left(\frac{p_{out}}{p_s}\right) - 1.0851\left(\frac{A_{mix}}{A_t}\right) + 0.0304\omega$

Where:
$m_{s,ad} = \frac{m_s(R*T_s)^{0.5}}{p_s A_{s,out}}$.
$Z = \omega\left(\frac{p_{mix}}{p_s}\right)^{0.02}$.
$Z' = \left(\frac{d_t}{d_{mix}}\right)^{0.1}(1+\omega)^{0.35}$.

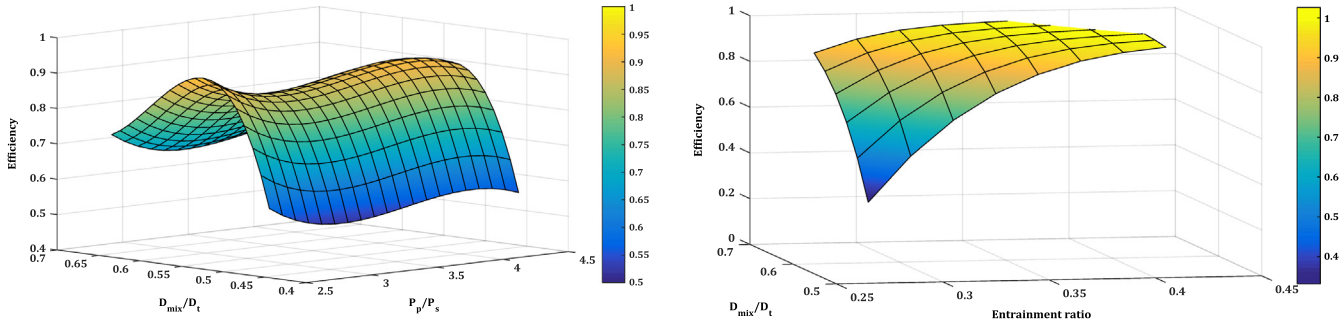

(a) Primary nozzle efficiency (b) Mixing chamber efficiency

Fig. 11. Primary nozzle and Mixing chamber efficiency maps provided by Liu and Groll [18].

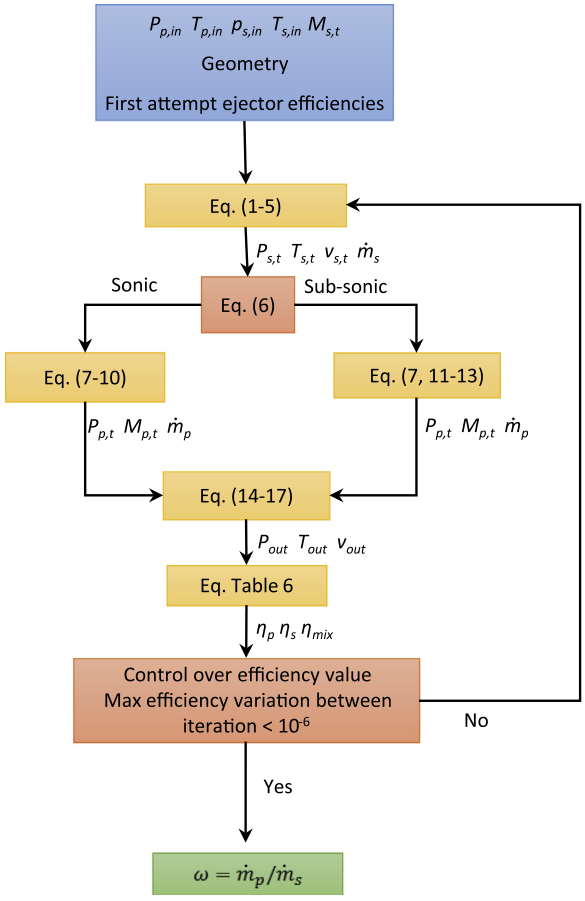

Fig. 12. ILPM-CFD solving procedure.

efficiency updating could be used for improving model stability, if needed. When the convergence is reached, the entrainment ratio is evaluated $\omega = \dot{m}_s/\dot{m}_p$. A sensitivity analysis on the first attempt ejector efficiencies was performed and showed that results do not depend upon the initial guess.

6.3. ILPM-CFD validation and evaluation

6.3.1. Validation and evaluation procedure

In order to validate and evaluate this model, both experimental and CFD data are used. At first, the ILPM-CFD and LPM-CE models were used to reproduce the experimental data previously used for validating the CFD approach (Table 2). Later, the comparison with CFD results is performed. ILPM-CFD performances are compared with the performance of LPM with Constant Efficiencies (LPM-CE). These models are built with the same structure of the ILPM-CFD, but without implementing a variable form for ejector efficiencies. Hence only Eqs. (1–13) are solved in a sequential way keeping constant ejector efficiencies. In the following, four LPM-CE models have been considered with the following efficiencies:

(1) LPM-CE #1: $\eta_p = 0.9$ and $\eta_s = 0.9$.
(2) LPM-CE #2: $\eta_p = 0.501$ and $\eta_s = 0.722$.
(3) LPM-CE #3: $\eta_p = 0.5$ and $\eta_s = 0.9$.
(4) LPM-CE #4: $\eta_p = 0.9$ and $\eta_s = 0.7$.

In general, all these values are representative of the most common efficiencies used (Table 7) and are in the range of variability reported in the literature [18,19]. The reader should also refer to the review of Liu [14] concerning the ejector component efficiencies used in lumped parameter models. The value of efficiencies for LPM-CE#1, were chosen to be representative of most common literature ejector efficiencies. The values for LPM-CP#2 were chosen in order to have a LPM-CE that best fits experimental data. In particular, the values of the LPM-CP#2 efficiencies were obtained by using the minimum mean square error method. The values for LPM-CE #3 and #4 were chosen to show the influence of a variation of η_p and η_s over ω and their value was chosen according to [18]. The reader may refer to the Table 7 for the summary concerning the ejector component efficiencies used in the previous literature.

6.3.2. Validation and evaluation using experimental data

The results summarized in Fig. 13 shows that ILPM-CFD fits the experimental data well. Among the LPM-CE models, only the LPM-CE#2 is able to fit experimental data. This is because its efficiencies were calibrated over experimental data. The average deviation between experimental data and ILPM-CFD, LPM-CE #1, LPM-CE #2, LPM-CE#3 model results are 0.59%, 20.35%, 0.87%, 10.29% and 36.46%, respectively.

These results can be used for some considerations on the effect of nozzle efficiencies η_p and η_s, considering models LPM-CE #3 and 4 and using as a reference LPM-CE #1. Decreasing η_p, the entrainment ratio decreases. This is because the primary nozzle is subject (given the boundary conditions) to a certain compression ratio β. Hence, if η_p is lower, $\dot{m}_p$ would increase for achieving the same β. Decreasing η_s, the entrainment ratio would increase. This is because in this model structure the suction chamber compression is given. Hence, a decrease in the suction chamber efficiency lead to a decrease of $\dot{m}_s$ (5) and an increase of $p_{s,t}$ (7). This may lead to the passage of the ejector from a critical (sonic) to a subcritical (subsonic) operating condition, with a consequent decrease of $\dot{m}_p$.

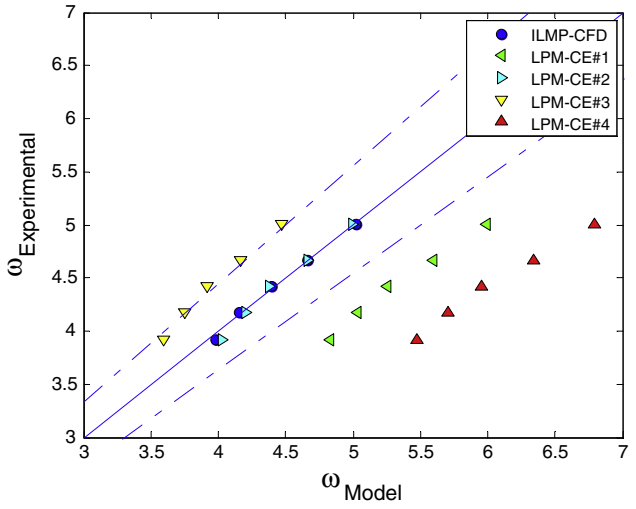

Fig. 13. Comparison between experimental data and model results; lines indicate ±10% of error.

6.3.3. Validation and evaluation using CFD data

Additional CFD simulations were performed for evaluating ILPM-CFD and LPM-CE models in a wide range of operating conditions. CFD results were compared with model results. Before presenting comparison results, it is worth noting, that a model comparison can be performed only if models have the same framework. In this case, the same framework means the same boundary conditions: pressure-inlet based models. Hence, these additional CFD simulations have pressure-inlet boundary conditions. Two situation ($p_{s,in}$ = 101,325 Pa and $p_{s,in}$ = 202,650 Pa) were investigated with following ranges:

- $p_{s,in}$ = 101,325 Pa and $1.05 \leqslant p_{p,in}/p_{s,in} \leqslant 6.75$;
- $p_{s,in}$ = 202,650 Pa and $1.55 \leqslant p_{p,in}/p_{s,in} \leqslant 6.75$.

The results (Fig. 14) shows that ILPM-CFD fits the CFD results fairly well in both conditions. Moreover, ILPM-CFD shows better performance compared to LPM-CE models. The average derivations between CFD data and ILPM-CFD, LPM-CE #1, LPM-CE #2, LPM-CE#3, LPM-CE#4 model results are:

- 0.75%, 13.74%, 6.23%, 15.20% and 28.99% for $p_{s,in}$ = 101,325 Pa;
- 0.51%, 15.44%, 7,62%, 13,99% and 30,84% for $p_{s,in}$ = 202,650 Pa.

For the case $p_{s,in}$ = 101,325 Pa the LPM-CE#2 was able to correctly fit CFD results in a limited range, but cannot predict the data in the whole operating range analyzed. This is because its efficiencies were calibrated over experimental data (Section 6.3.1, Fig. 13) using the minimum mean square error method. Indeed, experimental data concerns only a limited range of operating conditions, whereas CFD data concerns a larger range of operating conditions. In particular, the experimental data concerned the operating range (Table 2), which is well fitted by the LPM-CE#2 in Fig. 14. For the case $p_{s,in}$ = 202,650 Pa none of the LPM-CE models was able to fit CFD results, whereas ILPM-CFD is able to fits CFD results fairly well. This is because the ejector component efficiencies vary significantly (Fig. 15) in the range of analysis. This confirms that LPM-CE models are unable to reproduce ejector operating condition in the whole operating field. Therefore, LPM-CE models should be used carefully: they should be used only for tan evaluation of an ejector in on-design operation mode or in a very narrow range of operating conditions. In the latter case efficiencies should be care-fully evaluated before using the model. On the other side, ILMP-CFD is able to calibrate the value of efficiency in each operating condition. For this reason ILMP-CFD give the global parameter ω taking into account local flow behavior. The good behavior of the ILPM-CFD model is due to the great care in the validation process. Therefore, the ILPM-CFD model is able to take into account both the On-design and the Off-design operating conditions. The correct modeling of the Off-design operating conditions is possible not only for the LPM model structure (which takes into account the sonic and sub-sonic condition of the primary nozzle), but mainly for the variable ejector component efficiencies (that takes into account the local flow phenomena in the different operating condition).

7. Conclusions

This paper presents an Integrated Lumped Parameter-CFD model for ejector performance evaluation. The purpose of this approach is to evaluate the entrainment ratio, for a fixed geometry, for both on-design and off-design operating conditions. This model is illustrated with the case of a convergent nozzle ejector. Model results are compared with constant efficiency models, showing

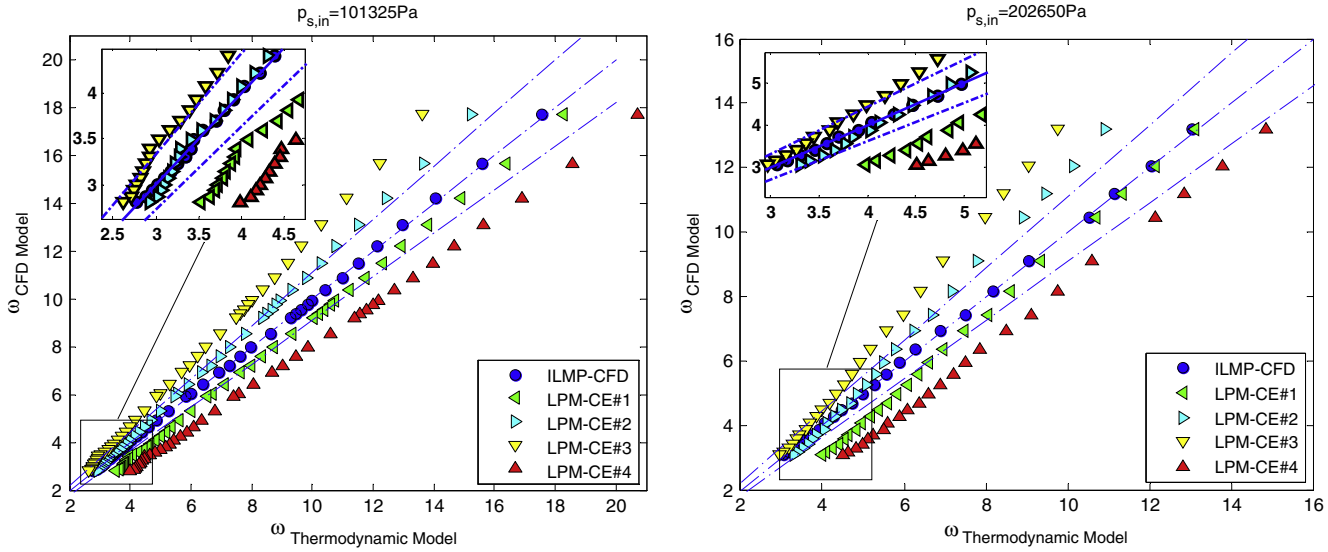

Fig. 14. Comparison between CFD and model results; lines indicate ±10% of error.

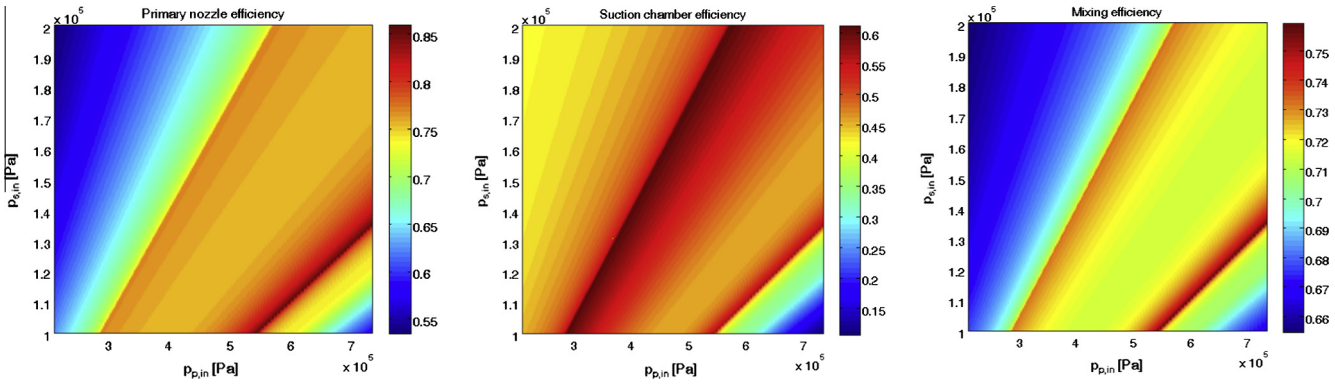

Fig. 15. Ejector efficiencies for the considered ejector – ILPM-CFM output for the considered operating range.

better performance and a wider range of applicability. The paper was structured in 4 parts. Each part has provided some advancement with respect to the literature.

At first, the numerical approach is validated by global and local data and seven RANS models are compared based on flow field, thermal field prediction and convergence capability. The k–ω SST model show the best performance and has been used in the other parts of the paper.

At second, a lumped parameter model for a subsonic ejector has been developed. This model can be coupled with variable efficiency or can be used with constant efficiency values.

At third, the CFD approach is used to investigate the flow field, to analyze its influence on ejector component efficiencies and to propose efficiency maps linking local flow quantities to ejector component efficiencies. η_p, η_s and η_{mix} range from 0.50 to 0.95, from 0.10 to 0.65, and 0.65 to 0.90, respectively: this range is larger if compared to the constant values found in the literature.

In the last part, the ejector efficiency maps are embedded into the lumped parameter model, thus developing the Integrated LPM-CFD model. The model has been validated and evaluated over experimental and CFD data. Moreover this model has been compared with constant efficiency model: the ILPM-CFD has shown better performance and a wider range of applicability. Constant efficiency models should be used carefully and only either in the evaluation of an ejector in on-design operation mode or in a very narrow range of operating conditions. In the latter case efficiencies should be carefully evaluated before using the model.

In conclusion, ejector component efficiencies have a great influence over ejector model accuracy and cannot be taken as constant. Ejector efficiencies can be applied for considering the local phenomena in LMPs by using efficiency maps. ILPM-CFD has the potentiality of coupling the advantages of both lumped parameter and CFD modeling techniques: accounting for local flow behavior with a lower time consuming model. Further developments are needed for improving this modeling approach. At first, the number of points for building efficiency maps is matter of further study. At second, further investigations are planned for investigating the influence of geometry and working fluid over ejector efficiencies. At third, future studies will apply this model to other datasets in order to expand the applicability of this approach to other case studies. Finally, the ILPM-CFD model can be used for studying off-design systems, where ejector efficiencies are not constant. In the future, the ejector model should be coupled with the models of the other components in the systems.

Acknowledgments

The authors would like to thank the anonymous reviewers for their valuable comments and suggestions to improve the quality of the paper.

Appendix A. Turbulence models convergence behavior

Considering fixed the discretization scheme, the grid density, and the numerical methods the computing time mainly depends upon the turbulence model used. In particular, we have analyzed the turbulence models considering:

(i) number of iterations needed;
(ii) CPU time required for a single iteration;
(iii) CPU time required for the whole simulation.

The first factor is related to the interaction between the turbulence model and the flow field. The second factor is related to the number of equations of the model and to the degree of nonlinearity of the equations. The last factor gives a sort of ranking of the suitability of turbulence model in terms of both convergence velocity and suitability for the flow field. The sensitivity analysis has been carried out using the Run 9 (reported in Table 2) and the numerical setup reported in Section 2. The methodology used here is well known in literature and specifically we referred to El-Behery and Hamed [81]. In the present analysis, we have taken the k–ε Standard as the baseline that requires 9942 iterations to reach the convergence. The results are shown in Table 4.

A.1. Number of iterations

The k–ε RNG and the k–ε Realizable require −7.35% and −5.46% than the k–ε Standard (total of 9942 iterations), respectively. This is because their mathematical structure is more adequate for jet mixing. The k–ω Standard reached the convergence slowly, with higher number of iterations compared to the baseline (+1.32% iterations). Indeed, the k–ε Standard has been developed for a benchmark closer to the present one with respect to the k–ω Standard. The k–ω SST requires −5.3% of iterations. Indeed, this model, thanks to its two-layer structure has a broad field of applications. The Spalart–Allmaras requires −6.65% of iterations. This is because the model has been built for aerospace applications. Finally, the RSM requires −1.98% of iterations than the baseline despite the higher number of equations used.

A.2. CPU time for iteration

The k–ε Realizable and the k–ε RNG models require more effort than the k–ε Standard (+19.46% and +2.37%, respectively) because of the extra terms in the equations. The k–ε RNG requires more time for iteration compared to the k–ε Realizable because of the closure coefficients. The k–ω Standard requires slightly more time for iteration (+3.89%) and the k–ω SST model requires about 2.01% greater time than the k–ω Standard (and about +6.09% compared

to the k–ε Standard) because of the extra functions associated with the mathematical formulation of the model. It is worth noting that despite of the comparable CPU time per iteration, the k–ω Standard requires about 6.67% greater time than that of k–ω SST. Finally, the RSM model requires a large time and number of iterations because of the extra transport equations to be solved. However, the RSM requires a slightly less time for iteration compared to the k–ε RNG: this is because we are solving a two dimensional problem and, therefore, the RSM model adds a limited number of transport equation.

A.3. Total CPU time

The k–ε Realizable and the Spalart–Allmaras showed the best performances. The Standard k–ε and the k–ω SST have comparable performance, followed by the k–ω Standard. The k–ε RNG and the RSM showed slow convergence reaching. This parameter is considered a compromise between the computational effort and the suitability of the models for the present flow fields.

References

[1] Little AB, Bartosiewicz Y, Garimella S. Visualization and validation of ejector flow field with computational and first-principles analysis. J Fluids Eng 2015;137:051107.
[2] Engelbracht M, Peters R, Blum L, Stolten D. Comparison of a fuel-driven and steam-driven ejector in solid oxide fuel cell systems with anode off-gas recirculation: part-load behavior. J Power Sources 2015;277:251–60.
[3] He S, Li Y, Wang RZ. Progress of mathematical modeling on ejectors. Renew Sustain Energy Rev 2009;13:1760–80.
[4] Besagni G, Mereu R, Inzoli F. CFD study of ejector flow behavior in a blast furnace gas galvanizing plant. J Therm Sci 2015;24:58–66.
[5] Zhu Y, Li Y. New theoretical model for convergent nozzle ejector in the proton exchange membrane fuel cell system. J Power Sources 2009;191:510–9.
[6] Maghsoodi A, Afshari E, Ahmadikia H. Optimization of geometric parameters for design a high-performance ejector in the proton exchange membrane fuel cell system using artificial neural network and genetic algorithm. Appl Therm Eng 2014;71:410–8.
[7] Dadvar M, Afshari E. Analysis of design parameters in anodic recirculation system based on ejector technology for PEM fuel cells: a new approach in designing. Int J Hydrogen Energy 2014;39:12061–73.
[8] Zhu Y, Li Y, Cai W. Control oriented modeling of ejector in anode gas recirculation solid oxygen fuel cell systems. Energy Convers Manage 2011;52: 1881–9.
[9] Keenan H, Neumann EP, Lustwerk F. An investigation of ejector design by analysis and experiment. J Appl Mech 1950:299–309.
[10] Zhu Y, Cai W, Wen C, Li Y. Shock circle model for ejector performance evaluation. Energy Convers Manage 2007;48:2533–41.
[11] Zhu Y, Cai W, Wen C, Li Y. Fuel ejector design and simulation model for anodic recirculation SOFC system. J Power Sources 2007;173:437–49.
[12] Zhu Y, Li Y. Novel ejector model for performance evaluation on both dry and wet vapors ejectors. Int J Refrig 2009;32:21–31.
[13] Hyun Im J, Jin Song S. Mixing and entrainment characteristics in circular short ejectors. J Fluids Eng 2015;137:051103.
[14] Liu F. Review on ejector efficiencies in various ejector systems. In: International refrigeration and air conditioning conference. Purdue; 2014.
[15] Aly NH, Karameldin A, Shamloul MM. Modelling and simulation of steam jet ejectors. Desalination 1999;123:1–8.
[16] Besagni G, Mereu R, Di Leo G, Inzoli F. A study of working fluids for heat driven ejector refrigeration using lumped parameter models. Int J Refrig 2015 [in press].
[17] Chen J, Havtun H, Palm B. Parametric analysis of ejector working characteristics in the refrigeration system. Appl Therm Eng 2014;69:130–42.
[18] Liu F, Groll EA. Study of ejector efficiencies in refrigeration cycles. Appl Therm Eng 2013;52:360–70.
[19] Varga S, Oliveira AC, Diaconu B. Numerical assessment of steam ejector efficiencies using CFD. Int J Refrig 2009;32:1203–11.
[20] Besagni G, Mereu R, Colombo E. CFD study of ejector efficiencies. In: ASME 2014 12th biennial conference on engineering systems design and analysis. American Society of Mechanical Engineers; 2014. p. V002T11A4–VT11A4.
[21] Pianthong K, Seehanam W, Behnia M, Sriveerakul T, Aphornratana S. Investigation and improvement of ejector refrigeration system using computational fluid dynamics technique. Energy Convers Manage 2007;48: 2556–64.
[22] Sharifi N, Boroomand M. An investigation of thermo-compressor design by analysis and experiment: Part 1. Validation of the numerical method. Energy Convers Manage 2013;69:217–27.
[23] Sharifi N, Boroomand M. An investigation of thermo-compressor design by analysis and experiment: Part 2. Development of design method by using comprehensive characteristic curves. Energy Convers Manage 2013;69: 228–37.
[24] Chandra VV, Ahmed MR. Experimental and computational studies on a steam jet refrigeration system with constant area and variable area ejectors. Energy Convers Manage 2014;79:377–86.
[25] Wang X, Dong J, Li A, Lei H, Tu J. Numerical study of primary steam superheating effects on steam ejector flow and its pumping performance. Energy 2014;78:205–11.
[26] Zhu Y, Jiang P. Experimental and numerical investigation of the effect of shock wave characteristics on the ejector performance. Int J Refrig 2014;40:31–42.
[27] Zhu Y, Jiang P. Experimental and analytical studies on the shock wave length in convergent and convergent–divergent nozzle ejectors. Energy Convers Manage 2014;88:907–14.
[28] Bartosiewicz Y, Aidoun Z, Mercadier Y. Numerical assessment of ejector operation for refrigeration applications based on CFD. Appl Therm Eng 2006;26:604–12.
[29] Gagan J, Smierciew K, Butrymowicz D, Karwacki J. Comparative study of turbulence models in application to gas ejectors. Int J Therm Sci 2014;78:9–15.
[30] Chen J, Jarall S, Havtun H, Palm B. A review on versatile ejector applications in refrigeration systems. Renew Sustain Energy Rev 2015;49:67–90.
[31] Gilbert GB, Hill PG. Analysis and testing of two-dimensional slot nozzle ejectors with variable area mixing sections. NASA; 1973.
[32] Versteeg HK, Malalasekera W. An introduction to computational fluid dynamics: the finite volume method. Pearson Education; 2007.
[33] Ansys FLUENT 13 – Theory guide. Ansys FLUENT2010.
[34] Bartosiewicz Y, Aidoun Z, Desevaux P, Mercadier Y. CFD-experiments integration in the evaluation of six turbulence models for supersonic ejectors modeling. Integrating CFD and Experiments. Glasgow; 2003. p. 71–8.
[35] Bouhanguel A, Desevaux P, Gavignet E. 3D CFD simulation of supersonic ejector. In: International seminar on ejector/jet-pump technology and application. Louvain-La-Neuve, Belgium; 2009.
[36] Dvorak V, Vit T. Experimental and numerical study of constant area mixing. In: 16th international symposium on transport phenomena. Prague; 2006.
[37] Kolář J, Dvořák V. Verification of K–ω SST turbulence model for supersonic internal flows. World Acad Sci, Eng Technol 2011;81:262–6.
[38] Georgiadis NJ, Chitsomboon T, Zhu J. Modification of the two-equation turbulence model in NPARC to a Chien low Reynolds number k–epsilon formulation. NASA; 1994.
[39] Sriveerakul T, Aphornratana S, Chunnanond K. Performance prediction of steam ejector using computational fluid dynamics: Part 2. Flow structure of a steam ejector influenced by operating pressures and geometries. Int J Therm Sci 2007;46:823–33.
[40] Zhu Y, Cai W, Wen C, Li Y. Numerical investigation of geometry parameters for design of high performance ejectors. Appl Therm Eng 2009;29:898–905.
[41] Georgiadis NJ, DeBonis JR. Navier–Stokes analysis methods for turbulent jet flows with application to aircraft exhaust nozzles. Prog Aerosp Sci 2006;42: 377–418.
[42] Han X, Sagaut P, Lucor D. On sensitivity of RANS simulations to uncertain turbulent inflow conditions. Comput Fluids 2012;61:2–5.
[43] Yang X, Ma H. Linear and nonlinear eddy-viscosity turbulence models for a confined swirling coaxial jet. Numer Heat Transfer, Part B: Fund 2003;43: 289–305.
[44] Kenzakowski D, Papp J, Dash S. Evaluation of advanced turbulence models and variable Prandtl/Schmidt number methodology for propulsive flows. In: 38th aerospace sciences meeting and exhibit. Reno, NV; 2000.
[45] Abdol-Hamid KS, Pao SP, Massey SJ, Elmiligui A. Temperature corrected turbulence model for high temperature jet flow. J Fluids Eng 2004;126: 844–50.
[46] Huang BJ, Chang JM, Wang CP, Petrenko VA. A 1-D analysis of ejector performance. Int J Refrig 1999;22:354–64.
[47] Hsia Y-C, Krothapalli A, Baganoff O. Mixing of an underexpanded rectangular jet ejector. J Propul Power 1988;4:256–62.
[48] Koita T, Iwamoto J. A study on flow behavior inside a simple model of ejector. In: International conference on fluid control, measurement and visualisation. Moskow, Russia; 2009.
[49] Colonna P, van der Stelt TP. FluidProp: a program for the estimation of thermo physical properties of fluids. The Netherlands: Energy Technology Section, Delft University of Technology; 2004.
[50] Rao SMV, Jagadeesh G. Novel supersonic nozzles for mixing enhancement in supersonic ejectors. Appl Therm Eng 2014;71:62–71.
[51] Papamoschou D, Johnson AD. Mixing enhancement from severely overexpanded nozzles. Int J Aerosp Innov 2010;2:235–52.
[52] Rao SM, Jagadeesh G. Observations on the non-mixed length and unsteady shock motion in a two dimensional supersonic ejector. Phys Fluids 2014;26:036103.
[53] Besagni G, Mereu R, Colombo E, Chiesa P, Maddiotto D. The influence of operating conditions and working fluids over ejector efficiencies: a CFD study. In: 32th UIT conference. Pisa, Italy; 2014. p. 1–10.
[54] Brunner DA, Marcks S, Bajpai M, Prasad AK, Advani SG. Design and characterization of an electronically controlled variable flow rate ejector for fuel cell applications. Int J Hydrogen Energy 2012;37:4457–66.
[55] Banasiak K, Palacz M, Hafner A, Buliński Z, Smołka J, Nowak AJ, et al. A CFD-based investigation of the energy performance of two-phase R744 ejectors to recover the expansion work in refrigeration systems: an irreversibility analysis. Int J Refrig 2014;40:328–37.

[56] Eames IW, Aphornratana S, Haider H. A theoretical and experimental study of a small-scale steam jet refrigerator. Int J Refrig 1995;18:378–86.
[57] Sun D-W. Variable geometry ejectors and their applications in ejector. Energy 1996;21:919–29.
[58] Grazzini G, Mariani A. A simple program to design a multi-stagejet-pump for refrigeration cycles. Energy Convers Manage 1998;39:1827–34.
[59] Huang BJ, Chang JM. Empirical correlation for ejector design. Int J Refrig 1999;22:379–88.
[60] Sun D-W. Comparative study of the performance of an ejector refrigeration cycle operating with various refrigerants. Energy Convers Manage 1999;40:873–84.
[61] Rogdakis ED, Alexis GK. Design and parametric investigation of an ejector in an air-conditioning system. Appl Therm Eng 2000;20:213–23.
[62] Cizungu K, Mani A, Groll M. Performance comparison of vapour jet refrigeration system with environment friendly working fluids. Appl Therm Eng 2001;21:585–98.
[63] Alexis GK, Rogdakis ED. A verification study of steam-ejector refrigeration model. Appl Therm Eng 2003;23:29–36.
[64] Selvaraju A, Mani A. Analysis of an ejector with environment friendly refrigerants. Appl Therm Eng 2004;24:827–38.
[65] Yapıci R, Ersoy HK. Performance characteristics of the ejector refrigeration system based on the constant area ejector flow model. Energy Convers Manage 2005;46:3117–35.
[66] Li D, Groll EA. Transcritical CO2 refrigeration cycle with ejector-expansion device. Int J Refrig 2005;28:766–73.
[67] Yu J, Chen H, Ren Y, Li Y. A new ejector refrigeration system with an additional jet pump. Appl Therm Eng 2006;26:312–9.
[68] Deng J-Q, Jiang P-X, Lu T, Lu W. Particular characteristics of transcritical CO2 refrigeration cycle with an ejector. Appl Therm Eng 2007;27:381–8.
[69] Godefroy J, Boukhanouf R, Riffat S. Design, testing and mathematical modelling of a small-scale CHP and cooling system (small CHP-ejector trigeneration). Appl Therm Eng 2007;27:68–77.
[70] Yu J, Li Y. A theoretical study of a novel regenerative ejector refrigeration cycle. Int J Refrig 2007;30:464–70.
[71] Yu J, Zhao H, Li Y. Application of an ejector in autocascade refrigeration cycle for the performance improvement. Int J Refrig 2008;31:279–86.
[72] Sarkar J. Optimization of ejector-expansion transcritical CO2 heat pump cycle. Energy 2008;33:1399–406.
[73] Elbel S, Hrnjak P. Experimental validation of a prototype ejector designed to reduce throttling losses encountered in transcritical R744 system operation. Int J Refrig 2008;31:411–22.
[74] Fangtian S, Yitai M. Thermodynamic analysis of transcritical CO2 refrigeration cycle with an ejector. Appl Therm Eng 2011;31:1184–9.
[75] Cardemil JM, Colle S. A general model for evaluation of vapour ejector performance for application in refrigeration. Energy Convers Manage 2012;64:79–86.
[76] Liu F, Groll EA, Li D. Modeling study of an ejector expansion residential CO2 air conditioning system. Energy Build 2012;53:127–36.
[77] Vereda C, Ventas R, Lecuona A, Venegas M. Study of an ejector-absorption refrigeration cycle with an adaptable ejector nozzle for different working conditions. Appl Energy 2012;97:305–12.
[78] Manjili FE, Yavari MA. Performance of a new two-stage multi-intercooling transcritical CO2 ejector refrigeration cycle. Appl Therm Eng 2012; 40:202–9.
[79] Kasperski J, Gil B. Performance estimation of ejector cycles using heavier hydrocarbon refrigerants. Appl Therm Eng 2014;71:197–203.
[80] Goodarzi M, Gheibi A, Motamedian M. Comparative analysis of an improved two-stage multi-inter-cooling ejector-expansion trans-critical CO2 refrigeration cycle. Appl Therm Eng 2015;81:58–65.
[81] El-Behery SM, Hamed MH. A comparative study of turbulence models performance for separating flow in a planar asymmetric diffuser. Comput Fluids 2011;44:248–57.